Earth and Space Science

RESEARCH ARTICLE
10.1029/2024EA004070

**Key Points:**

- We analyzed particulate inorganic and organic carbon (PIC and POC) from satellites, in situ optics and pumps N Pacific to Southern Ocean
- 0–500 m PIC sensor data reveals deep euphotic zone maxima not detected by satellites and strong export at mid-latitudes and equator
- Sensor and satellite optical methods misidentify "PIC" in the Antarctic; chain-forming diatom cavities may cause anomalous optical signals

**Supporting Information:**

Supporting Information may be found in the online version of this article.

**Correspondence to:**

J. K. B. Bishop,
jkbishop@berkeley.edu

**Citation:**

Li, Y., Bishop, J. K. B., Lam, P. J., & Ohnemus, D. C. (2025). Analysis of satellite and in situ optical proxies for PIC and POC during GEOTRACES GP15 and GP17-OCE transects from the subarctic north Pacific to the Southern Ocean. *Earth and Space Science*, *12*, e2024EA004070. https://doi.org/10.1029/2024EA004070

Received 4 NOV 2024
Accepted 13 MAR 2025

**Author Contributions:**

**Conceptualization:** Yunhao Li, James K. B. Bishop
**Data curation:** James K. B. Bishop
**Formal analysis:** Yunhao Li, James K. B. Bishop, Daniel C. Ohnemus
**Funding acquisition:** James K. B. Bishop, Phoebe J. Lam, Daniel C. Ohnemus
**Investigation:** Yunhao Li, James K. B. Bishop, Phoebe J. Lam
**Methodology:** Yunhao Li, James K. B. Bishop
**Project administration:** James K. B. Bishop, Phoebe J. Lam, Daniel C. Ohnemus
**Resources:** James K. B. Bishop, Phoebe J. Lam, Daniel C. Ohnemus



# Analysis of Satellite and In Situ Optical Proxies for PIC and POC During GEOTRACES GP15 and GP17-OCE Transects From the Subarctic North Pacific to the Southern Ocean

**Yunhao Li[1], James K. B. Bishop[1], Phoebe J. Lam[2], and Daniel C. Ohnemus[3]**

[1]Earth and Planetary Science, University of California, Berkeley, CA, USA, [2]Ocean Sciences, University of California, Santa Cruz, CA, USA, [3]Department of Marine Sciences, Skidaway Institute of Oceanography, University of Georgia, Savannah, GA, USA

**Abstract** The biological pump, a fundamental process governing atmospheric $CO_2$, rapidly transfers particulate inorganic and organic carbon (PIC and POC) from surface waters to the deep sea but is inherently highly variable in space and time, and thus poorly observed. Here we synthesize PIC and POC data from satellites, CTD-profiled optical sensors (birefringence and transmissometer), and from in situ pumps samples from GEOTRACES transects spanning 20,000 km from the North Pacific to Southern Ocean. High resolution profile data from PIC sensors revealed strong subsurface maxima in the deepest euphotic zone waters of oligotrophic gyres; furthermore, data showed high concentrations of PIC penetrating to >500 m south of the Subarctic Front (45°N–35°N), at the equator, and north of the Antarctic Polar Front (45°S–55°S) indicating high carbon export in these regions. We developed a new temporal/spatial interpolation scheme for satellite data that improved matchups with ship observations. North of the Antarctic Polar Front (APF), PIC sensor data was generally well aligned with sample PIC; however, a positive bias of satellite PIC was found in poor retrieval regions. South of the APF, both satellite and birefringence sensor greatly overestimated PIC by factors of >25 and 12, respectively, compared to sample PIC which averaged 15 nM. The unanticipated discovery of a non-carbonate particle birefringence source coupled with a microscopic investigation of pump samples leads us to hypothesize that internal reflection within bubbles and/or cellular structures of heavily silicified colony-forming diatoms (*Fragilariopsis* and *Pseudo-nitzschia*) is the cause for anomalous birefringence and adds to backscattered satellite radiances.

**Plain Language Summary** Atmospheric $CO_2$ levels are influenced by fast biological processes in the ocean. Prediction requires an understanding of how biological processes create and transfer particulate inorganic and organic carbon (PIC and POC) to depth, yet observations are sparse. Here we synthesize satellite and GEOTRACES ship observations from Adak, Alaska to the frigid waters near 67°S in the Southern Ocean. Along the transect north of the Antarctic Polar Front (APF) near 55°S, PIC and POC concentrations — measured surface to 500 m depth — using novel particle birefringence sensors and transmissometers yielded data consistent with analyses of simultaneously collected samples in most cases; satellite PIC data were based high in cloudy areas. The new PIC sensor revealed unseen detail of deep dwelling coccolithophore populations in subtropical gyres and mid-latitude and equatorial zones of enhanced particle transfer to depth. An unanticipated discovery was a strong overestimation of PIC by sensor (and even more so by satellites) south of the Antarctic Polar Front in surface waters colder than 1°C. We hypothesize that buoyancy promoting voids formed by some members of living colony-forming *Fragilariopsis* and *Pseudo-nitzschia* diatoms are the source of biases found. In contrast, satellite and sensor POC data were little affected across the APF transition.

## 1. Introduction

The ocean biological carbon pump (OBCP) (Volk & Hoffert, 1985), is both fast and dynamic and is an important factor governing the uptake of atmospheric $CO_2$ by the ocean; yet it is poorly observed. Globally, 1–2 Pg of oceanic photo synthesizers produce organic carbon at a rate of ~50 Pg C $yr^{-1}$ (Falkowski & Raven, 2007; Field et al., 1998), with actions of consumers leading to an export of carbon —primarily by sinking particles (Boyd et al., 2019) — at uncertain rates from 5 to 12 Pg C $yr^{-1}$ (Boyd & Trull, 2007; Clements et al., 2023; Henson et al., 2011; Siegel et al., 2014; Yao & Schlitzer, 2013). This process leads to a pH increase in surface waters which favors the uptake of atmospheric $CO_2$.

**Software:** Yunhao Li, James K. B. Bishop
**Supervision:** James K. B. Bishop, Phoebe J. Lam, Daniel C. Ohnemus
**Validation:** Yunhao Li, James K. B. Bishop, Phoebe J. Lam, Daniel C. Ohnemus
**Visualization:** Yunhao Li, James K. B. Bishop
**Writing – original draft:** Yunhao Li, James K. B. Bishop
**Writing – review & editing:** Yunhao Li, James K. B. Bishop, Phoebe J. Lam, Daniel C. Ohnemus

Calcareous phytoplankton synthesize particulate inorganic carbon (PIC) as a byproduct of photosynthesis at rates between 0.4 and 1.8 Pg C $yr^{-1}$ (Balch et al., 2016; Berelson et al., 2007; Feely et al., 2004). Calcification plays two roles in the OBCP. First, the packaging of PIC within sinking aggregates enhances their sinking rate and leads to reduced remineralization of particulate organic carbon (POC) in the mesopelagic zone (Armstrong et al., 2001). Second, the production of calcium carbonate lowers surface water alkalinity, which lowers pH and increases $pCO_2$ countering the effects of photosynthesis. Furthermore, the decreasing pH and calcium carbonate saturation state of surface waters from the uptake of anthropogenic $CO_2$ (Feely et al., 2009; Sabine et al., 2004) may short-circuit the OBCP by reducing calcification rates and aggregate sinking rates.

Remote sensing has provided a novel view of the global distributions of PIC within the first optical depth (37% light level, Gordon & McCluney, 1975) of the euphotic zone (Balch et al., 2005, 2018; Gordon et al., 2001; Mitchell et al., 2017). However, a large fraction of PIC in the euphotic zone is missed, and in the case of tropical and subtropical waters, coccolithophores can be found as deep as the 0.1% light level (Bishop et al., 2022; Okada & Honjo, 1973; Poulton et al., 2017).

Methods to measure PIC concentrations and fluxes are still limited. There are fewer than 150 PIC profiles extending from surface waters through the mesopelagic zone (Lam & Xiang, 2025; Lam et al., 2011, 2018) because large volume in situ filtration sampling is required for accurate measure of low PIC concentration waters (Bishop et al., 2022). Many such observations are temporally restricted to fair weather conditions and are spatially sparse due to their dependence on ships.

To understand the water column dynamics of PIC (and POC) and its role in carbon export, we have developed an autonomous float, the Ocean Carbon Observer (OCO, Bishop & Wood, 2024), equipped with both an optical sedimentation recorder (OSR, Bishop, 2009; Bourne et al., 2021) and particle concentration sensors that measure both transmissometer beam attenuation coefficient as a proxy for POC (Bishop et al., 1998) and particle birefringence as an optical proxy for PIC (Bishop et al., 2022). The OCO profiles and drifts between 0 and 1,000 m to yield diurnal variations of PIC and POC concentrations and fluxes with depth.

The optical sensors for PIC and POC were profiled surface to bottom along two GEOTRACES transects: GP15 from Adak Alaska to Tahiti (2018, 152°W, 56°N to 20°S), and GP17-OCE (Hereafter: GP17) from Tahiti to the Southern Ocean (20°S to 67°S). Together, the expeditions sampled biologically diverse regimes, including the subarctic north Pacific, oligotrophic north and south Pacific gyres, the Pacific equatorial regime, the Subantarctic Frontal Zone ("The Great Calcite Belt"; Balch et al., 2011, 2016; Patil et al., 2017), the circumpolar current, and the coldest waters of the Southern Ocean (Figure 1).

Resulting data for 77 stations has enabled a comprehensive synthesis and analysis of PIC and POC from remote sensing, CTD (Conductivity Temperature Depth) deployed optical sensors, and from samples collected by large volume in situ filtration, the latter which serve as both "surface truth" and "in situ truth" for both sets of optical proxies.

## 2. Materials and Methods

PIC and POC data were obtained in three ways during this study. First, CTD interfaced sensors for particle birefringence and particle beam attenuation coefficient were deployed to full water column depth (Section 2.1). Second, PIC and POC samples were collected by McLane large volume in situ pump deployments at the same stations and analyzed ashore at the University of California, Santa Cruz (Section 2.2). Third, we matched ship observations with satellite retrieved values PIC and POC (Section 2.3).

### 2.1. CTD Data

During both GP15 and GP17, birefringence sensor PIC011, and transmissometer CST1450 were interfaced to the Seabird 19-plus logging CTD and deployed during McLane pump casts; data were recorded at 14-bit resolution at 4 Hz; similarly, sensors PIC010 and CST1035 were deployed interfaced to a SBE 911 CTD on the GEOTRACES Trace Element Sampling Carousel (GTC) and recorded at 12-bit resolution at 24 Hz. Transmissometer CST1874 was deployed on the Ocean Data Facility (ODF) CTD/rosette system during GP17 (12-bit, 24 Hz).

Optical data obtained during CTD deployments were despiked by iteratively computing the mean and standard deviation (s.d.) of data over 10 s intervals and excluding data that fall outside of ±3 s.d. Limits (Bishop et al., 2022).

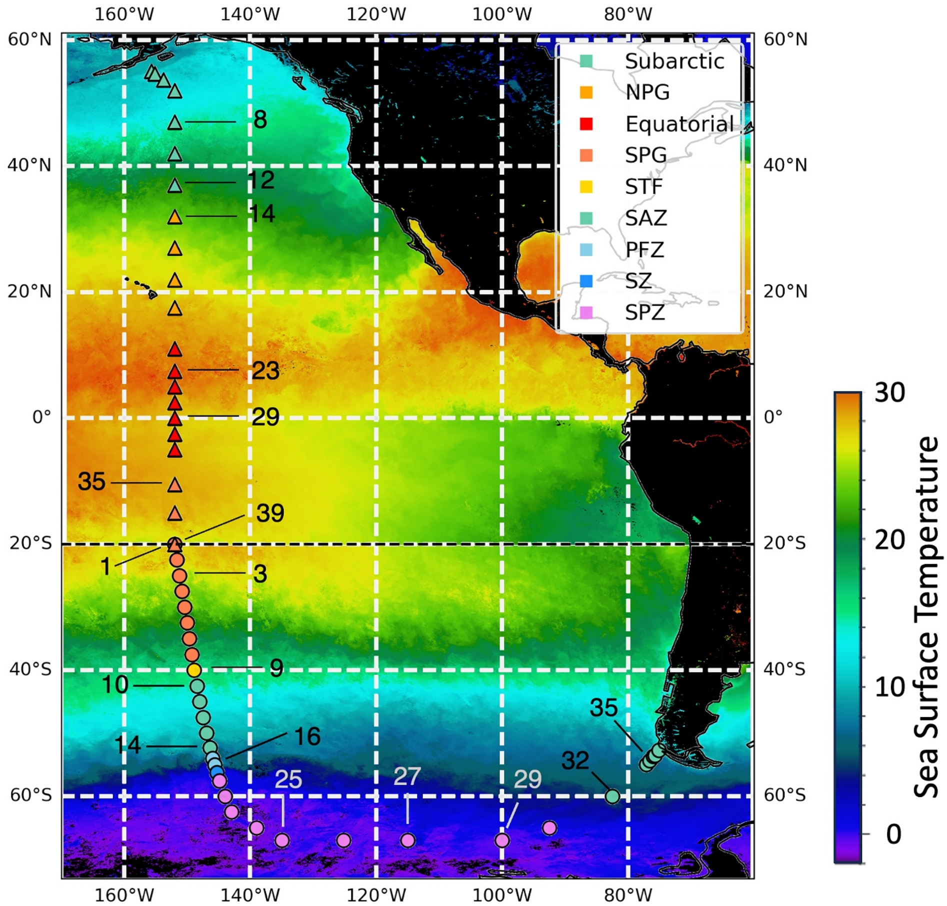


**Figure 1.** Spatial distribution of stations occupied during GP15 from Adak, Alaska to Tahiti in 2018 (triangles) and GP17-OCE from Tahiti to the Southern Ocean in 2022/2023 (circles). Colored legend symbols and acronyms for biogeochemical regimes and front positions are defined in Table 2. Locations overlay MODIS AQUA sea surface temperature maps for Oct 2018 (from 60°N to 20°S) and for 19 Dec 2022, to 19 Jan 2023 (South of 20°S). The Antarctic Polar Front lies between GP17 stations 16 and 18.

In discussions of transects of optically derived PIC and POC concentrations to 500 m, we use the average of all profiles at each station. In describing profile details at each station and match ups with McLane data, we use data from separate CTD casts. We note that sensor data are robust to full water column depth but we limit discussion to the upper 500 m in this paper.

### 2.1.1. PIC Sensor

The two PIC sensors (PIC010, and PIC011) used in this study have been extensively documented (Bishop et al., 2022). Briefly, the sensors are built on a digital WETLabs C-star 25 cm pathlength 6,000 m rated transmissometer. A 660 nm laser replaced the transmissometer's light emitting diode (LED) light source. High crossing efficiency polarizers were externally mounted to both source and receiver windows; the source polarizer is aligned with the plane of polarization of the laser and the receiver polarizer is crossed to minimize transmission of the direct beam. When light from the primary beam encounters birefringent particles, its plane of polarization is rotated, and the sensor receives a signal. Although detailed methodology is published (Bishop et al., 2022) an abbreviated description is included in supplemental materials (Text S1 in Supporting Information S1) which describes the transformation of raw sensor voltages read by the CTD into the sensor independent quantity, birefringent photon yield, $\beta_{corr}$, with units of ppm m$^{-1}$. $\beta_{corr}$ is converted to PIC (in nM) by multiplying by 15 (in units - nM ppm$^{-1}$ m; Bishop et al., 2022); we refer to this quantity as "birefringence PIC" or "PIC$_{\beta}$."

#### 2.1.2. Transmissometer POC

During GP15, transmissometer CST1450 was the standard for beam attenuation coefficient ($c_p$) for the entire section as it was both stable and air calibrated prior to each deployment; the other transmissometers were adjusted to this standard. CST1874 on the ODF-CTD was used as a standard for GP17. GP15 and GP17 $c_p$ values are accurate to better than 0.01 $m^{-1}$, and systematically precise to better than 0.003 $m^{-1}$. Additional detail is found in Text S2 in Supporting Information S1.

Transmissometer POC (in μM) is calculated by multiplying $c_p$ by 27 (Bishop & Wood, 2008), derived from regression of the sum of POC in three nominal size fractions (0.8–1.2, 1.2–51 μm, and >51 μM) sampled using the Multiple Unit Large Volume in situ Filtration System (MULVFS), against $c_p$. We refer to this Proxy as "$POC_{cp0.8}$."

#### 2.1.3. First Attenuation Depth Averaging of $PIC_\beta$ and $POC_{cp0.8}$

Averaged diffuse attenuation coefficient ($Kd_{490}$) from AQUA, TERRA, and SNPP satellites was used to compute the first attenuation depths representative of satellite data (Gordon & McCluney, 1975); these attenuation depths ($z = 1/Kd_{490}$) ranged from 9 to 49 m. At each station, $PIC_\beta$ and $POC_{cp0.8}$ data were averaged over the corresponding depth in order to compare with satellite results.

### 2.2. In Situ Particle Sampling and Analysis

McLane pumps deployed during GEOTRACES filtered several hundred liters in surface waters to 1,000 L in deep waters. Dried samples were analyzed ashore. The deployment procedures for the McLane Research in situ Water Transfer System (WTS) Large Volume (LV) pumps are described by Xiang and Lam (2020). Typically, eight pumps were deployed with a logging CTD to confirm sampling depths. At GP17 S16 (55°S, 145.66°W) on 25 Dec 2022, the *R/V Revelle* was hit by a rogue wave. Extreme ship roll led to the loss of eight McLane pumps, the CTD, and sensors PIC011 and CST1450. Contemporaneous data $PIC_\beta$ from PIC011 and samples are available at S1, S3, S6, S12, and S14. Stations GP17 S8 and S10 had pump samples but had no useful CTD recorded sensor data. Thus, profile comparisons with McLane samples at GP17 S8, S10, S20, S22, S25, S27, S29, S35 and S37 rely on non-contemporaneous data from PIC010 onboard the GTC CTD.

Each pump carried two 142 mm diameter filter holders, each with two separate filter stages with multiple baffles upstream of the filters to ensure even particle distribution and to prevent particle loss (Bishop et al., 2012). One filter holder was configured with a 51 μm Sefar polyester mesh prefilter followed by paired Whatman QMA quartz fiber filters. The second filter holder was configured with the same Sefar 51 μm prefilter but followed by paired 0.8 μm Pall Supor polyether sulfone filters. These holders are referred to as the "QMA" and "SUPOR" holders, respectively. Particle analyses reported in this paper are primarily from the QMA holder. In some cases, we refer to analyses of subsamples from the "SUPOR" holder.

Sample analytical results and methodology for GP15 are documented by Lam et al. (2024a, 2024b). Identical methods were used during GP17. Here we report Particulate inorganic carbon (PIC) as measured by coulometry. We refer to PIC determined in 1–51 μm and >51 μm fractions as $PIC_S$ and $PIC_L$, respectively and the sum of these fractions as $PIC_{S+L}$.

### 2.3. Satellite OBCP Proxies

#### 2.3.1. Data Sources and Calculation of $PIC_{CI2}$

Satellite retrievals of sea surface chlorophyll-a (Hu et al., 2012), PIC (2B/3B algorithm, Balch et al., 2005; Gordon et al., 2001), and POC (Stramski et al., 2008) at 4 km 8 day temporal resolution from AQUA MODIS (Moderate Resolution Imaging Spectroradiometer) and TERRA MODIS and SNPP VIIRS (Visible Infrared Imaging Radiometer Suite) were downloaded in June 2023 from the NASA ocean color level 3 (L3) data browser (https://oceancolor.gsfc.nasa.gov/l3/). Standard Satellite POC and PIC products are referred to as $POC_{SAT}$ and $PIC_{2B/3B.}$

Level 3 Color Index 2-band (CI2, Mitchell et al., 2017) PIC products derived from level 2 data are available but are not contemporaneous with GEOTRACES. For this reason, we produced our own CI2 PIC product (hereafter, $PIC_{CI2}$) using level 3 (L3) reflectance data (Rrs547 and Rrs667 for MODIS, Rrs551 and Rrs671 for VIIRS). We

**Table 1**
*Definition of Terms Used in This Paper for PIC and POC as Optical Proxies and Analyzed Quantities*

| Abbreviation | Units | Definition |
|---|---|---|
| $PIC_{\beta}$ | nM | PIC from CTD birefringence sensors (Bishop et al., 2022) |
| $POC_{cp0.8}$ | μM | POC from CTD beam attenuation coefficient (>0.8 μm) (Bishop & Wood, 2008) |
| $PIC_{S+L}$ | nM | PIC concentration from McLane samples (sum of 1–51 μm (*S*) and >51 μm (*L*) particle size fractions). |
| $PIC_{2B/3B}$ | nM | PIC concentration from remote sensing: 2 band/3 band algorithm (Balch et al., 2005; Gordon et al., 2001) |
| $PIC_{CI2}$ | nM | PIC concentration from remote sensing: band difference algorithm (Color Index, Mitchell et al., 2017) |
| $POC_{SAT}$ | μM | POC concentration from remote sensing: (Stramski et al., 2008) |

believe this calculation is reasonable in the case of GEOTRACES match ups (Text S3 in Supporting Information S1).

#### 2.3.2. Satellite Data Reprocessing

For this study, we have developed an improved scheme using 8-day composite data that achieves a more complete and more accurate spatial and temporal match up of ship and satellite data (Text S4 in Supporting Information S1). The scheme was validated against matchups calculated using daily imagery over 3 days which bracket the time of ship observations (Text S5 in Supporting Information S1). The spatial-temporal scheme is tested by linear regression of 3-versus 8-day SST, chlorophyll-a, PIC, and POC (Text S6 in Supporting Information S1), all of which showed high correlation and slopes close to 1.

**Table 2**
*Grouping for Stations Along in GP15 and GP17-OCE Cruises*

| Cruise | Position | Station(s) | Region/Fronts |
|---|---|---|---|
| GP15 | 55°N–37°N | 3–9 | Subarctic |
| | | 10–12 | Subarctic Frontal Zone |
| | 32°N–17.5°N | 14–19 | North Pacific Gyre (NPG) |
| | 11°N–5°S | 21–33 | Equatorial Regime |
| | 10.5°S–20.0°S | 35–39 | South Pacific Gyre (SPG) |
| GP17 | 20.0°S–27.5°S | 1–8 | |
| | | 9 | Subtropical Front (STF) |
| | 37.5°S–52.3°S | 10–14 | Subantarctic Zone (SAZ) |
| | | | Subantarctic Front (SAF) |
| | 54°S–55°S | 15–16 | Polar Frontal Zone (PFZ) |
| | | | Antarctic Polar Front (APF) |
| | | | Southern ACC front (sACCF) |
| | 56.3°S | 18 | Southern Zone (SZ) |
| | | | ACC Southern Boundary (SB) |
| | 57.6°S–67°S, 144.9°W–92.5°W | 20–30 | Subpolar Region (SPZ) |
| | | | ACC Southern Boundary (SB) |
| | | | Southern ACC front (sACCF) |
| | | | Antarctic Polar Front (APF) |
| | | | Subantarctic Front (SAF) |
| | 60°S–52.5°S, 82.5°W–75.1°W | 32–38 | Subantarctic Zone (SAZ) |

#### 2.3.3. Summary of Optics Terms Used in This Manuscript

See Table 1.

## 3. Results

### 3.1. Hydrographic Context and Grouping Logic for GP15 and GP17 Transect

The Pacific GP15 transect from 56°N to 20°S along 152°W started in Alaskan shelf and subarctic high-nutrient low-chlorophyll (HNLC) waters, crossed the oldest deep water in the North Pacific gyre and the equatorial upwelling region, and ended in the ultra-oligotrophic waters in the South Pacific Gyre. The GP17 transect (Figure 1) consisted of three legs: from 20°S to 67°S along ∼152–135°W, a zonal transect at 67°S from 135°W to 100°W, and a northeast bound section (100°W–75°W, 55°S). GP17 sampled waters from the strongly oligotrophic South Pacific gyre to the highly productive Antarctic polar region crossing several Antarctic Frontal Zones. Together, the transects sampled surface waters ranging in temperature from −0.5°C to 29°C. Stations are classified into groups based on their hydrographic and biogeochemical characteristics which are summarized in Table 2 (Orsi et al., 1995; Talley et al., 2011; Twining et al., 2023).

### 3.2. Validation of Satellite 8 Day Composite Match-Up Scheme

Figure 2 shows SST from three satellites and shipboard CTD casts along both transects. We confirmed consistency of shipboard along-track continuous flow SST data and CTD data which showed agreement to better than 0.1°C. Diurnal SST variations on station were less than 0.3°C.

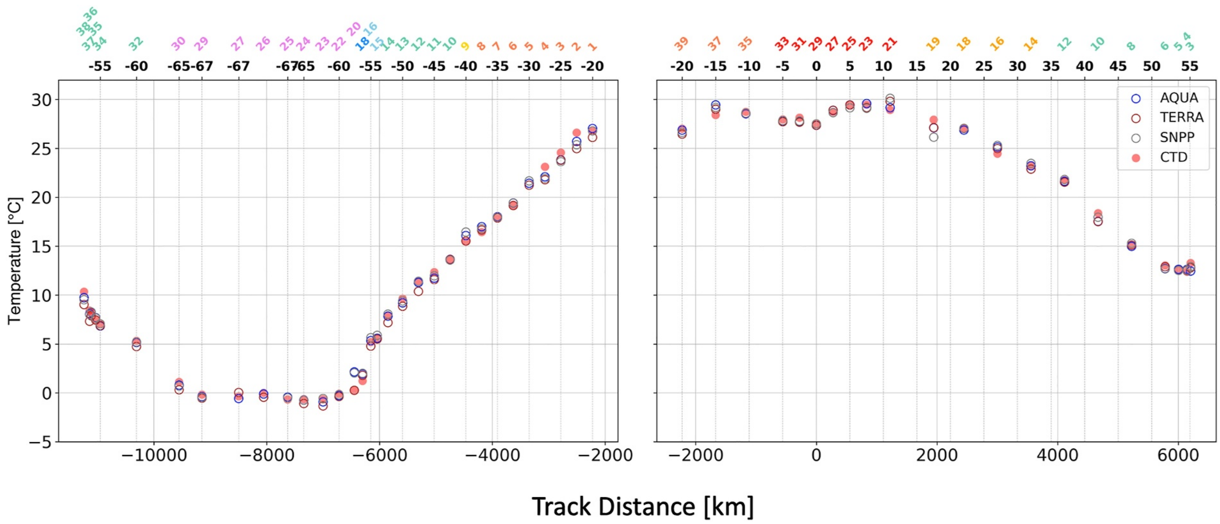


**Figure 2.** Retrievals of sea surface temperature (SST) from AQUA, TERRA, and SNPP using the improved 8 day composite are compared to in situ SST from CTD casts at stations along both transects. Left and right panels are GP17 and GP15, respectively. Ship track distance uses the equator as reference. Latitude and station numbers are at the top of the plot. The average of the along-track SST trend is used to provide a hydrographic reference in our discussion.

Figure 3 shows the statistics of SST anomaly computed using data derived from the continuously recording shipboard meteorological system (MET). Sea surface temperature was the most variable (>2°C) at GP17 S14, reflecting strong physical variability near the Subantarctic Front. For most stations, the difference between satellite SST, in situ SST, and CTD SST is less than 0.5°C. Where departures exceed a 0.5°C difference, results frequently showed satellite SST values colder than observations, suggesting the effects of clouds at sub pixel scale.

### 3.3. PIC Profiles During GP17

Comparisons of birefringence PIC ($PIC_\beta$) from sensors PIC010 and PIC011 with PIC analyzed in samples from McLane pumps ($PIC_{S+L}$) during GP15 have already been reported (Bishop et al., 2022), and for this reason we focus on profile comparisons during GP17.

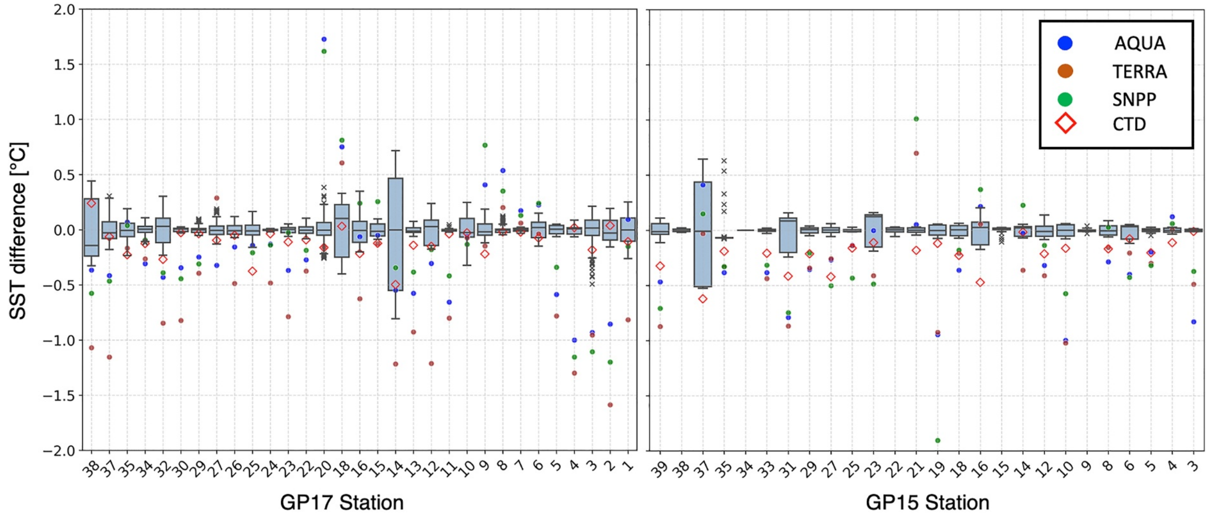


**Figure 3.** Sea surface temperature (SST) anomaly at GP15 and GP17 stations. Box plots show SST anomaly referenced to the mean of 6 min averaged data from the shipboard meteorological system (MET). Each box shows the 25, 50, 75 percentiles with error bars representing 0 and 100 percentiles; crosses mark the outliers. Similarly calculated are satellite SST anomaly and CTD SST anomaly.

10.1029/2024EA004070

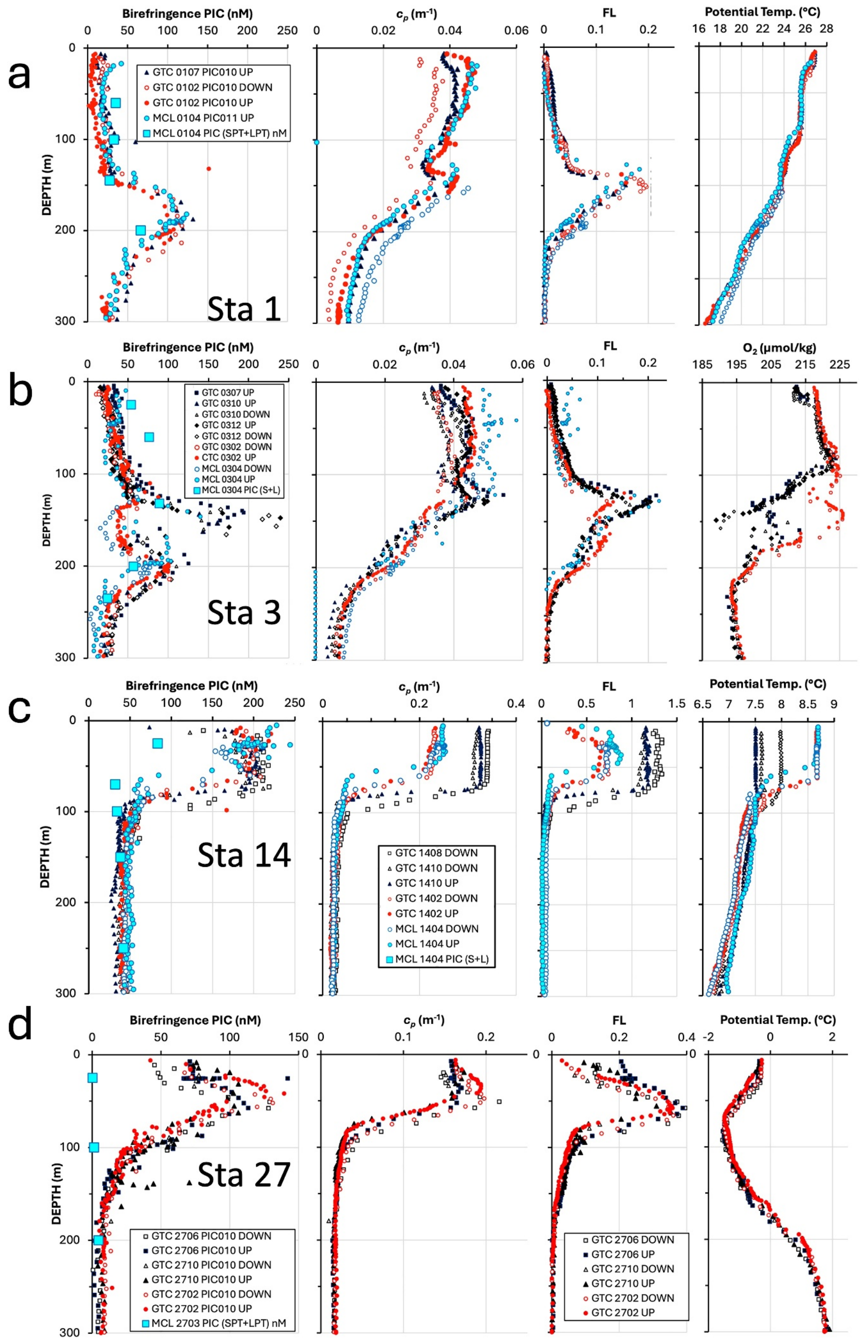


**Figure 4.** (a) Comparison of sensor $PIC_{\beta}$ and sample $PIC_{S+L}$ at station 1. McLane cast CTD (PIC011), and sample data are highlighted as filled cyan and open blue symbols. PIC010 data from the GTC CTD are also shown; red symbols denote casts closest to the time of McLane sampling. Also shown are the particulate organic carbon proxy beam attenuation coefficient ($c_p$, $m^{-1}$) and fluorometer data (in relative units), (b), (c), and (d) data for GP17 stations 3, 14, and 27. Hydrographic data are presented at the right side of each row of plots. The 25 m PIC value at S14 is based on analysis of material from the Supor sample.

Figure 4 shows $PIC_{\beta}$ and $PIC_{S+L}$ with profiles for beam attenuation coefficient and fluorescence at GP17 stations 1, 3, 14, and 27 (here after "station 1" will be "S1", etc.).

At South Pacific Gyre S1 and S3 (Figures 4a and 4b) $PIC_{\beta}$ and $PIC_{S+L}$ are in good agreement at McLane depths sampled. Also in agreement are profile and sample data from S6, S8 and S12. The subsurface maximum in PIC at

S1 was found approximately 40 m deeper than the fluorescence maximum at 190 m. At S3, $PIC_{\beta}$ near 150 m averaged 20 nM during McLane sampling but shifted to 240 nM in later profiles which reflected the intrusion of a lower oxygen (195 vs. 225 μmol $O_2$ $kg^{-1}$) water mass.

Near the Subantarctic Front, at S14 (Figure 4c) $PIC_{\beta}$ and $PIC_{S+L}$ are in excellent agreement at depths 70 m and deeper but a failure of the pump at 25 m to collect samples in the "QMA" filter holder meant that archival subsamples from the Supor filter holder were analyzed. This sample at 25 m yielded $PIC_{S+L}$ value of 83 nM, approximately 50% of the $PIC_{\beta}$ concentrations. S14 was remarkable for having strong temperature variability (Figure 3) and factor-of-two shifts of beam attenuation coefficient and fluorescence.

In the subpolar zone S27 (Figure 4d) is a clear-cut case where $PIC_{\beta}$ and $PIC_{S+L}$ were far different. There, Scanning Electron Microscope (SEM) and X-ray fluorescence (XRF) imaging of the QMA sample showed abundant diatoms and no evidence of carbonate particles. $PIC_{S+L}$ was lower than 4 nM at all depths sampled while $PIC_{\beta}$ exceeded 50 nM at depths sampled and peaked to 150 nM at 50 m. Stations S20, S22, S25 and S29 showed similar disagreements in near surface waters. There must be a signal independent from carbonate particle birefringence in the coldest of Antarctic waters.

### 3.4. Transmitted and Polarized Light Microscopy of Prefilter Samples at Stations 14 and 25

To understand the birefringence PIC signals at high latitudes in the Southern Ocean, we microscopically examined and imaged dried material from prefilter samples collected from 25 m at GP17 S14 and S25 under parallel and cross-polarized transmitted light (Figures 5a and 5b). We used available sample from S25 as it is hydrographically similar to S27 (Figure 4d). The sample from the Subantarctic Zone at S14 shows strongly birefringent foraminifera, coccolithophores. Also in the image are weakly birefringent dinoflagellates. At S25, there is a scant visible evidence for carbonate particles, consistent with McLane sample results, yet there is a birefringence signal arising from non-carbonate particles. Figure 5c shows attenuance and birefringence in the two samples as cumulative area weighted distributions summed from high to low. While attenuance loading of the two samples is nearly identical, S14 stands out in terms of its cumulative birefringence distribution, in other words, carbonates are a dominant source of birefringence in the samples.

Figure 6 shows a magnified view of the attenuance and birefringence (at longer exposure times) images of a sample from S25 under collimated (condenser out) and non-collimated (divergent, condenser in) light. What stands out in the cross polarized light imagery is that some of the diatoms appear to yield a polarization signal. We also noticed that this interference decreased over a period of 10 days (Figure S8 in Supporting Information S1) suggesting that immersion oil had slowly filled cavities in the diatoms. We hypothesize below that the anomalous $PIC_{\beta}$ profiles at stations 20 through 29 arise due to forward internal reflections within such cavities.

### 3.5. Ship and Satellite Transect Comparison

Figure 7a compares PIC from the three approaches along both GP15 and GP17: $PIC_{2B/3B}$ retrieved from satellites and both McLane sample $PIC_{S+L}$ and sensor PIC010 $PIC_{\beta}$ averaged over one attenuation depth. $PIC_{\beta}$, $POC_{cp0.8}$ and potential temperature sections to 500 m are shown in Figures 7b and 7d, respectively. These sections are overlaid with lines depicting mixed layer depth, fluorescence maximum, and euphotic zone depth to provide a hydrographic context.

In our plots, euphotic zone depth is defined as the depth below the fluorescence maximum where fluorescence falls to 10% of the maximum value and corresponds to the 1% light level (Owens et al., 2015). Mixed layer depth is calculated assuming a potential density anomaly difference of 0.05 units.

#### 3.5.1. Water Column Systematics

In the euphotic zone, highest birefringent $PIC_{\beta}$ occurs in waters shallower than 50 m in subarctic waters north of 47°N; south of the subarctic front, a subsurface maximum developed reaching depths near 120 m in the North Pacific Gyre (12.5°N–27.5°N). The Equatorial Zone showed highest values in near surface waters. In the South Pacific Gyre a $PIC_{\beta}$ maximum was found between 150 and 225 m at GP15 stations S33 to S39 and at GP17 S1 to S5 (5°S–30°S). Distributions at crossover stations at 20°S (GP15 S39 and GP17 S1), reproduce each other both in concentration systematics and in the fact that the $PIC_{\beta}$ maximum was found 40 m deeper than the fluorescence

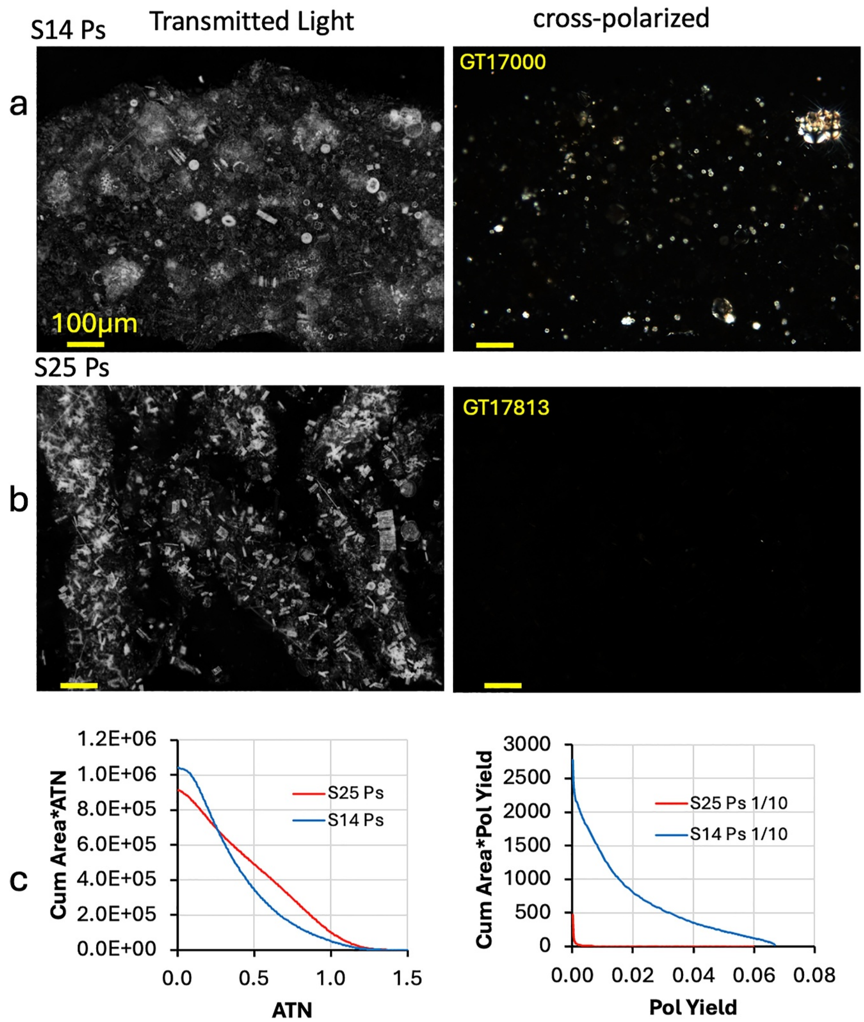


**Figure 5.** Comparison of Attenuance and Polarization Photon Yield images from GP17 Stations (a) 14, and (b) 25. Transmitted and cross polarized collimated illumination of the samples was used. Cumulative distributions of Attenuance ($Log_{10}$ of transmission) and Polarization Yield for the same samples are shown in (c). Scale bars are 100 μm.

maximum. Lowest $PIC_{\beta}$ values were observed at GP17 stations S6 to S8. Beginning at GP17 S9 the $PIC_{\beta}$ maximum and fluorescence maximum became superimposed and progressively shallowed to near surface waters. $PIC_{\beta}$ concentrations exceeding 1,000 nM were observed near 75 m at stations 15 and 16 in the Polar Frontal Zone. In the frigid waters of the Subpolar Region, a $PIC_{\beta}$ maximum was found in the upper 50 m with values ranging as high as 400 nM (S29); but concentrations strongly attenuated with depth to near zero values by 100 m. We noted above in Section 3.3 (Figure 4d) that $PIC_{S+L}$ was less than 2 nM in shallow waters while $PIC_{\beta}$ ranged between 100 and 140 nM at S27. We will show below that $PIC_{\beta}$ also overestimates $PIC_{S+L}$ values at GP17 S22, S25, S27, and S29. We have no samples to compare with at stations 15 through 20, nor any at stations 30 and 32.

In sub euphotic zone waters, $PIC_{\beta}$ distributions had relative minima at GP15 stations 6 and 7 (north of 50°N), at stations 21 and 22 (near 11°N) and at S33 (at 5°S) all reflecting oxygen depleted waters. Highest $PIC_{\beta}$ concentrations were found extending from the base of the euphotic zone to 500 m near 40°N just south of the subarctic front, at the equator, and just north of the Antarctic Polar Front suggesting strong PIC export at these latitudes.

Figure 7c shows the $POC_{cp0.8}$ transect to depths of 500 m. POC is highest in waters from 45°N to 55°N, near the equator, and south of 40°S. Enhanced concentrations of POC in sub euphotic zone waters is indicative of enhanced POC export (Bishop, 2009). In the Southern Zone at stations 18 and 20 both $PIC_{\beta}$ and $POC_{cp0.8}$ show

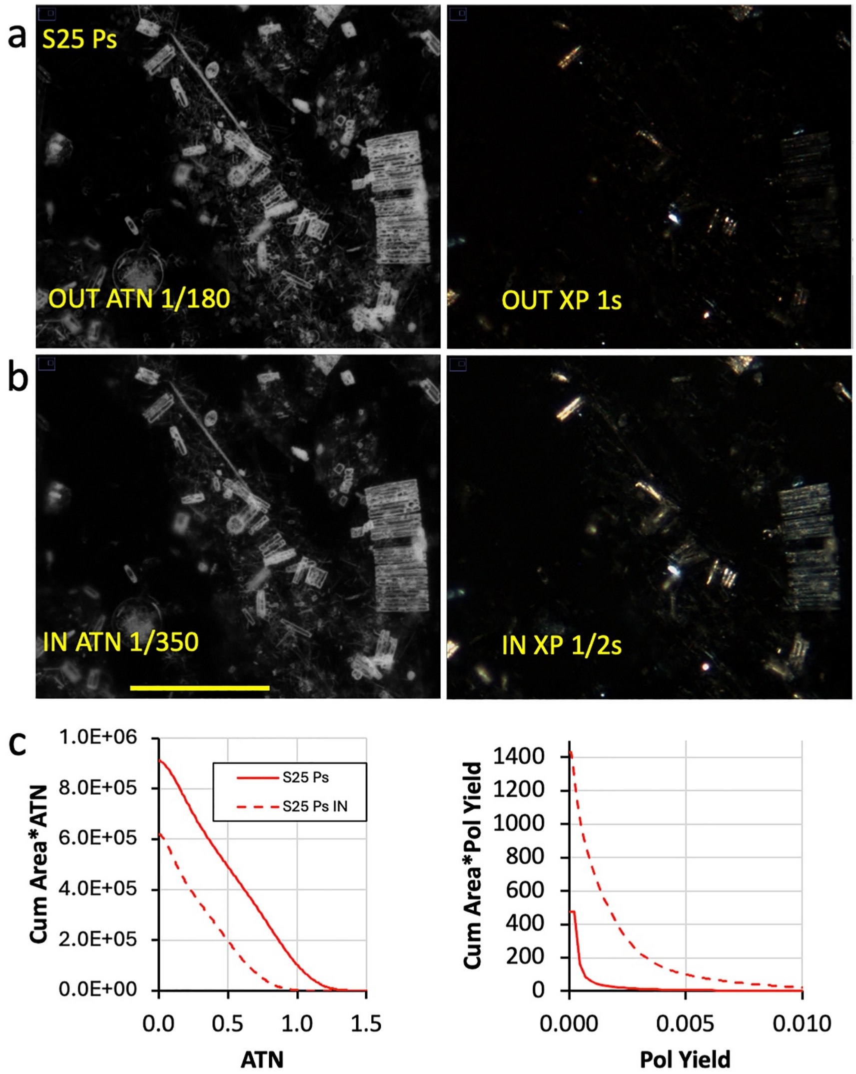


**Figure 6.** Comparison of Attenuance and Polarization Photon Yield images from GP17 Station 25 under (a) collimated, and (b) non-collimated (divergent) illumination. Much longer exposure times were used for images under cross-polarized illumination. Cumulative distributions of Attenuance (Log10 of transmission) and Polarization Yield for the same conditions are shown in (c). Scale Bar of 80 µm is shown.

relative minima in surface waters probably due to strong divergence of flow between the Southern Antarctic Circumpolar Current Front (sACCF) and SB.

### 3.5.2. Intercomparison of $PIC_{S+L}$, $PIC_{\beta}$ and $PIC_{2B/3B}$

Figure 7a compares McLane sample $PIC_{S+L}$ data and birefringent $PIC_{\beta}$ averaged over one attenuation depth along with the $PIC_{2B/3B}$ from three different satellites. In the subarctic, $PIC_{\beta}$ from sensor PIC010 and PIC011 is lower than McLane $PIC_{S+L}$ and $PIC_{2B/3B}$. We found good agreement between $PIC_{\beta}$, $PIC_{S+L}$, and $PIC_{2B/3B}$ in the oligotrophic gyre waters and equatorial regions where PIC concentration is below 50 nM. In the regions with suboptimal satellite coverage, there are a few cases (e.g., GP15 stations 19, 25 and 35; GP17 stations 3 and 5) where satellite PIC deviates well above 100 nM while sensor and sample PIC stay low. In GP17, $PIC_{S+L}$, and $PIC_{2B/3B}$ increase south of the Subtropical Front, followed by an elevation of upper layer PIC concentration.

Sensor $PIC_{\beta}$ generally agrees with sample $PIC_{S+L}$, and satellite $PIC_{2B/3B}$ in the Subantarctic Zone. There is an anomaly at GP17 S10, where $PIC_{\beta}$ profiles underestimate $PIC_{S+L}$ but in trends paralleling each other (Figure S9 in Supporting Information S1). GP17 S12 shows $PIC_{S+L}$ and $PIC_{\beta}$ in agreement. The highest PIC concentration

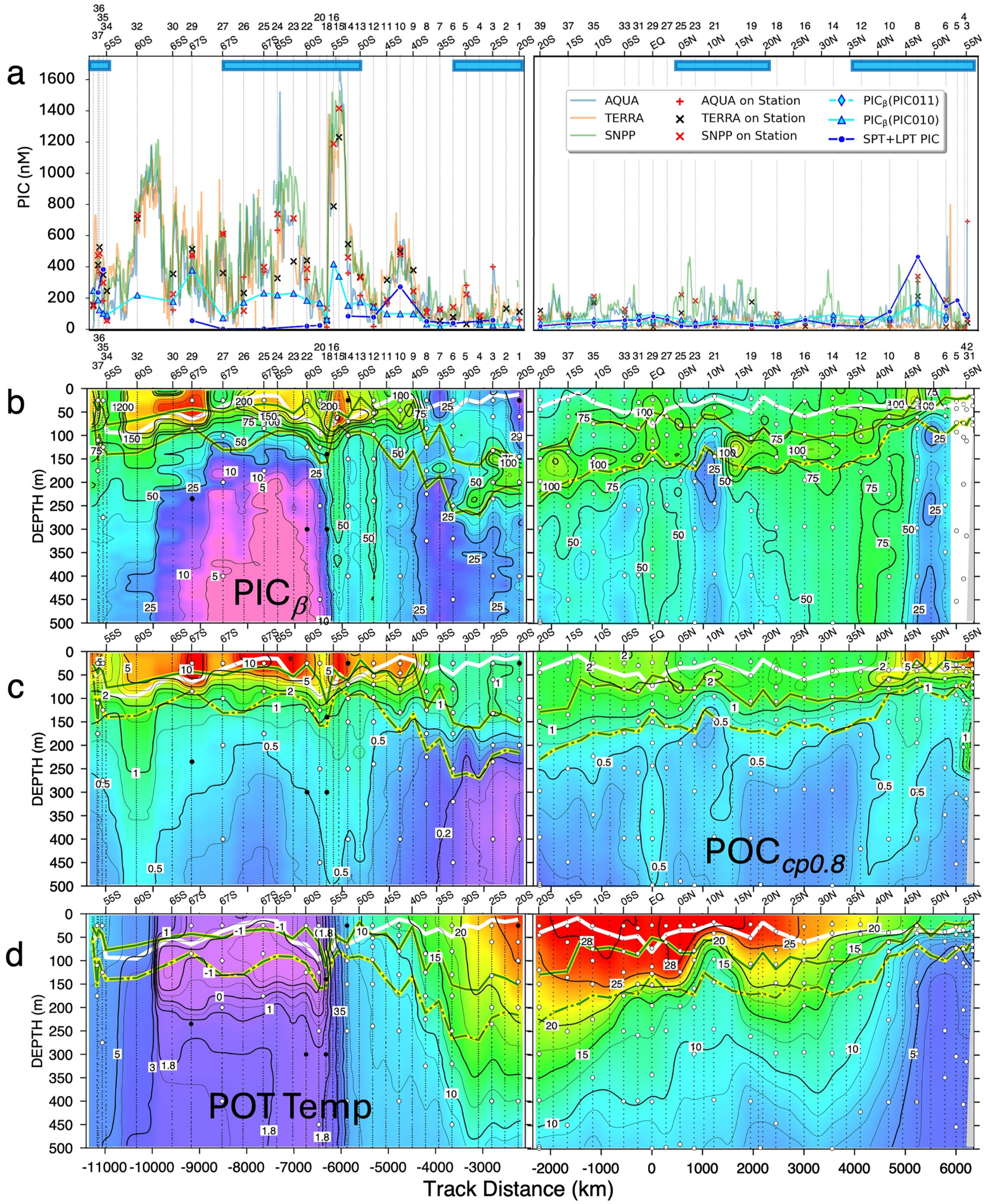
a
b
c
d
PIC (nM)
AQUA
TERRA
SNPP
AQUA on Station
TERRA on Station
SNPP on Station
PICβ(PIC011)
PICβ(PIC010)
SPT+LPT PIC
DEPTH (m)
PICβ
POCcp0.8
POT Temp
Track Distance (km)

**Figure 7.**

was seen in the Polar Frontal Zone at GP17 S15 and S16 where $PIC_{\beta}$ reached 400 nM. Here, $PIC_{2B/3B}$ exceeds $PIC_{\beta}$ by a factor of 2–3. No sample data are available at GP17 S16. In the Subpolar Region, $PIC_{S+L}$ is largely absent (averaging ~20 nM). Satellite derived $PIC_{2B/3B}$ averages 20 times higher than sample $PIC_{S+L}$. Sensor derived $PIC_{\beta}$ averages ~10 times higher than $PIC_{S+L}$ suggesting that non-carbonate particles in the Subpolar Region somehow produce a birefringence signal. In the Subantarctic Zone on the northeast bound transect of GP17 McLane $PIC_{S+L}$, $PIC_{\beta}$ and $PIC_{2B/3B}$ are generally aligned, as was found in the Subantarctic Zone during the southbound transect.

#### 3.5.3. Systematics of $PIC_{\beta}$, $PIC_{2B/3B}$, $PIC_{CI2}$ Versus $PIC_{S+L}$

To understand how well sensor birefringent $PIC_{\beta}$ and satellite $PIC_{2B/3B}$ compare with the in situ $PIC_{S+L}$ directly measured in the pump samples, Figures 8a–8c show plots of $PIC_{\beta}$ minus $PIC_{S+L}$, $PIC_{2B/3B}$ minus $PIC_{S+L}$, and $PIC_{CI2}$ minus $PIC_{S+L}$, respectively along the GEOTRACES transects. $PIC_{\beta}$ is lower than sample PIC by between 200 and 300 nM in subarctic waters at GP 15 S8 and at GP17 S10 and S35; we will discuss these stations below. $PIC_{\beta}$ averages 200 nM higher than $PIC_{S+L}$ in the near freezing waters of the Subpolar Region (S20 through S29) confirming unknown birefringence sources in these waters.

The trend of satellite $PIC_{2B/3B}$ minus $PIC_{S+L}$ (Figure 8b) is like the trend for $PIC_{CI2}$ minus $PIC_{S+L}$ (Figure 8c), but the latter is positively offset. $PIC_{2B/3B}$ is closer to the sample $PIC_{S+L}$ in the Pacific Gyres while $PIC_{CI2}$ agrees better with sample PIC in the subarctic north Pacific. The two algorithms strongly overestimate PIC in the Subpolar Region where SST is below 0°C; the bias of $PIC_{CI2}$ exceeds 700 nM at S27 and is approximately 30% higher than the bias of $PIC_{2B/3B}$.

### 3.6. Relationships Between $PIC_{\beta}$, $PIC_{2B/3b}$, and $PIC_{S+L}$

The regression analysis for match-ups of sensor $PIC_{\beta}$, satellite $PIC_{2B/3B}$, and McLane sample $PIC_{S+L}$ is shown in Figure 9. North of the APF, all properties are correlated. Satellite $PIC_{2B/3B}$ versus $PIC_{\beta}$ show the highest correlation (Figure 9a, $R^2 = 0.71$; Slope = 2.6 ± 0.3) compared with $PIC_{2B/3B}$ versus $PIC_{S+L}$ (Figure 9c; $R^2 = 0.49$, Slope = 0.8 ± 0.2), and $PIC_{\beta}$ versus $PIC_{S+L}$ (Figure 9e, $R^2 = 0.46$; Slope = 0.28 ± 0.13); $PIC_{\beta}$ in near surface waters underestimates $PIC_{S+L}$ by a factor of 3.

South of the APF, no correlation was found for either $PIC_{2B/3B}$ versus $PIC_{\beta}$ (Figure 9b, $R^2 = 0.12$) or $PIC_{2B/3B}$ versus $PIC_{S+L}$ (Figure 9d, $R^2 = 0.02$); in these waters, $PIC_{2B/3B}$ far exceeds $PIC_{S+L}$. We did find significant correlation of $PIC_{\beta}$ versus $PIC_{S+L}$ (Figure 9f, $R^2 = 0.71$, Slope 4.3 ± 1.6), but that $PIC_{\beta}$ overestimates $PIC_{S+L}$.

### 3.7. Surface Trends in Satellite and Sensor POC Proxies and Trends in Pigment Biomarkers

Figure 10a shows the intercomparison of satellite $POC_{SAT}$ with McLane sample $POC_{0.8S+L}$ (only GP15) and $POC_{cp0.8}$ averaged to the 37% light level. $POC_{cp0.8}$ from multiple transmissometers closely track one another across both GP15 and GP17 sections. $POC_{SAT}$ overestimates $POC_{0.8S+L}$ north of 50°N in the subarctic, while $POC_{cp0.8}$ and sample $POC_{0.8S+L}$ agree with each other. $POC_{cp0.8}$ and $POC_{0.8S+L}$ follow one another in the Pacific gyres and equatorial Pacific while $POC_{SAT}$ has a similar trend but is positively offset by 1.4 μM in the North Pacific Gyre. Similar offsets were found in the South Pacific Gyre. Such offsets are expected as a major fraction of photosynthetic biomass is in smaller than 0.8 μm in oligotrophic waters. $POC_{cp0.8}$ converges with $POC_{SAT}$ in the Subantarctic Zone and rises to approximately 30% higher than $POC_{SAT}$ in the Subpolar Region. POC maxima (10–12 μM) are found at S15 and S16 in the Polar Frontal Zone and in the Southern Zone.

Figures 10b and 10c show averaged and integrated inventories of diatom, coccolithophore, and dinoflagellate biomarkers within the euphotic zone to the first attenuation depth, respectively. For all GP15 and for GP17 to S11 (45°S), coccolithophore pigments trend higher than diatoms. Notable peaks in diatom biomarkers occur at S16

**Figure 7.** (a) Comparison of AQUA, TERRA, and SNPP satellite retrievals of surface layer PIC concentrations, PIC from one attenuation depth averaged McLane samples, and one attenuation depth averaged $PIC_{\beta}$ from sensor PIC010 (GP15&GP17) and from PIC011(GP15 only), (b) $PIC_{\beta}$ section from sensor PIC010, (c) $POC_{cp0.8}$, and (d) Potential temperature section. Left and Right Panels are from GP17 and GP15, respectively. The distance coordinate is track distance relative to the equator. Blue bars over top of Figure 8a mark regions with poor satellite retrieval. White line: mixed layer depth. Green solid and dashed lines: fluorescence maximum and base of euphotic zone depths, respectively.

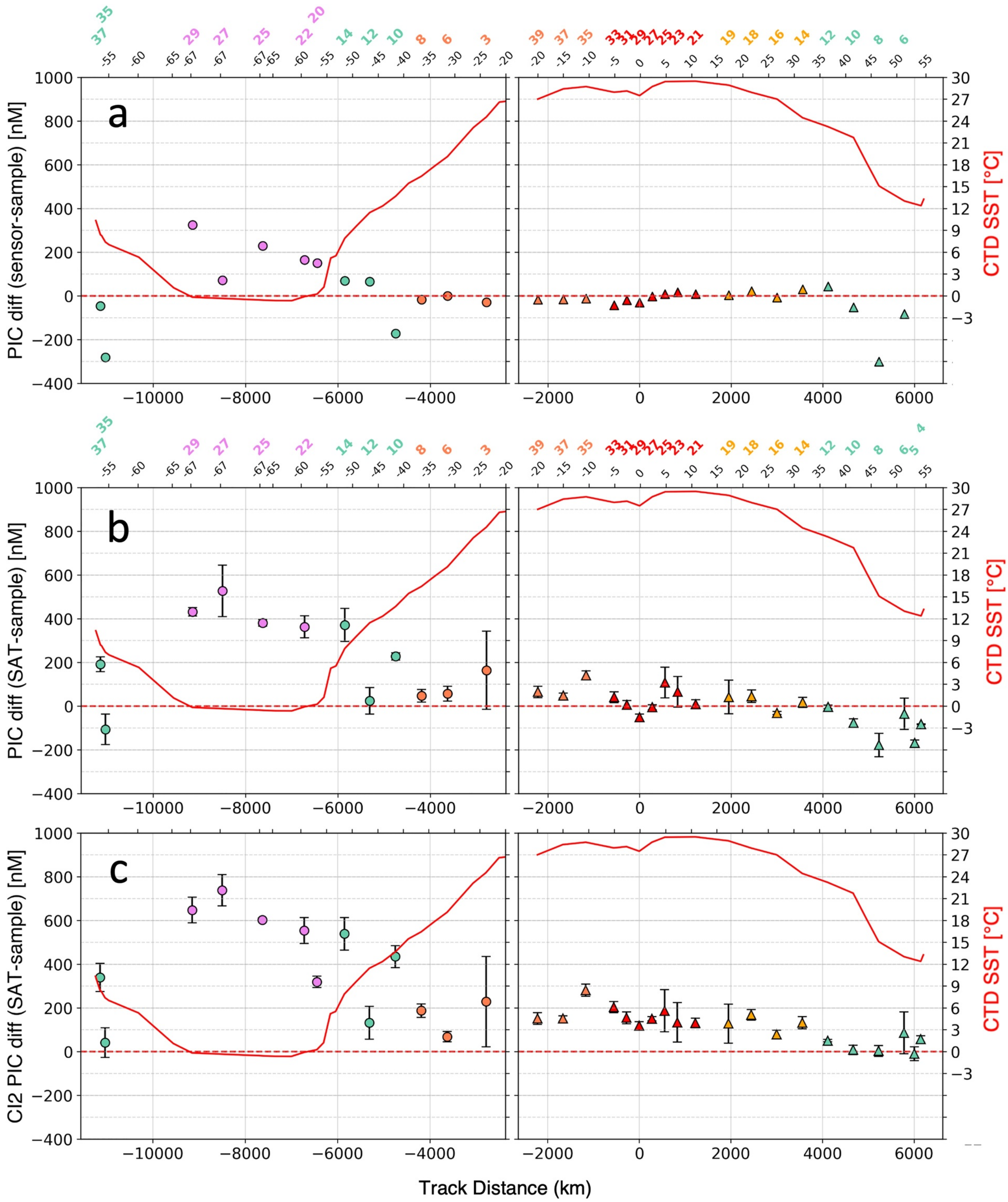

**Figure 8.** Differences (a) between sensor $PIC_{\beta}$ and McLane sample $PIC_{S+L}$, (b) between satellite $PIC_{2B/3B}$ (averaged from 3 satellites) and $PIC_{S+L}$, and (c) between $PIC_{CI2}$ (averaged from 3 satellites) and $PIC_{S+L}$. The datapoints are colored by their biogeochemical regions (Table 2). The red line marks the sea surface temperature (SST) from CTD. Error bars mark ±1 standard deviation. Track Distance is computed referenced to the equator. GP17 and GP15 are plotted in left and right panels. The measurement bias for both sensor PIC and satellite PIC increases as the SST drops below 1°C.

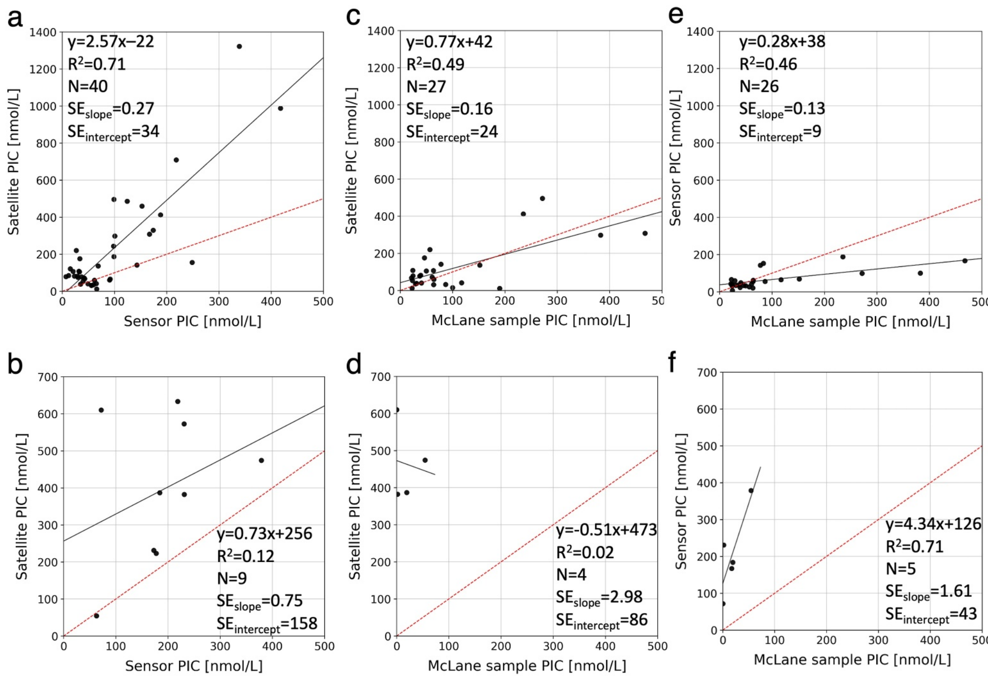


**Figure 9.** Regression and statistics between satellite $PIC_{2B/3B}$ (median of three satellites), $PIC_{\beta}$ (from PIC010), and McLane sample $PIC_{S+L}$ along the GP15 and GP17-OCE cruise track. Data are classified into north of APF (a, c, e) and the south of APF (b, d, f). The red line denotes a 1:1 relationship.

and S29 and high values are seen at S15, and at stations S22 through S30. Dinoflagellate-sourced pigment peridinin peaked at GP17 S13.

## 4. Discussion

### 4.1. Spatial Temporal Match Up

Our interpolation scheme improved the satellite data retrieval matchups where fractional clouds are present (Text S5 and S6 in Supporting Information S1, Figures S5, S6, and S7 in Supporting Information S1). The strong correlation between 8 day interpolated satellite SST and ship SST (Figures 2 and 3) indicates that our spatial-temporal interpolation scheme is robust across the entire section from 29°C strongly stratified waters to −0.5°C waters south of the Antarctic Polar Front. For OBCP parameters in the subarctic north Pacific, retrieval percentages were near 100% in original 8 day composites; however visual inspection of images shows strong disagreement among satellites and with the sample data (Figure S10 in Supporting Information S1). There, retrieved $PIC_{2B/3B}$ and $POC_{SAT}$ were noisy and exceed samples by 4 and 3 times, respectively (Figures 7a and 10a). By looking at the statistics of how multiple satellites agree with one another we conclude that there was a breakdown of retrievals at these latitudes at the time of GP15. At mid-latitudes, in low retrieval areas, there were 100–200 nM $PIC_{2B/3B}$ differences among satellites and results similarly exceed sample data. Such a multi-satellite statistical approach would flag bad PIC data; $POC_{SAT}$ was far less affected.

### 4.2. Comparison Between $PIC_{2B/3B}$ and $PIC_{CI2}$

Currently, the 2B/3B algorithm is the standard product for PIC provided by NASA Ocean Color Level 3 browser. The 2B/3B is a combination of two-band (blue-green) algorithm optimized for non-bloom concentrations of coccolithophores (Balch et al., 2005) and three-band red/near-infrared (NIR) algorithm optimized for turbid, high reflectance coccolithophore blooms (Gordon et al., 2001). The algorithm was combined into a switching algorithm (NASA Ocean Color PIC algorithm; link: https://oceancolor.gsfc.nasa.gov/resources/atbd/pic/). In version R2022, which we are using, $PIC_{2B/3B}$ was adjusted to account for the packaging effect of different coccolithophore classes versus coccoliths. The adjustment makes low $PIC_{2B/3B}$ values lower and high $PIC_{2B/3B}$ values higher, with a null shift at around 80 nM.

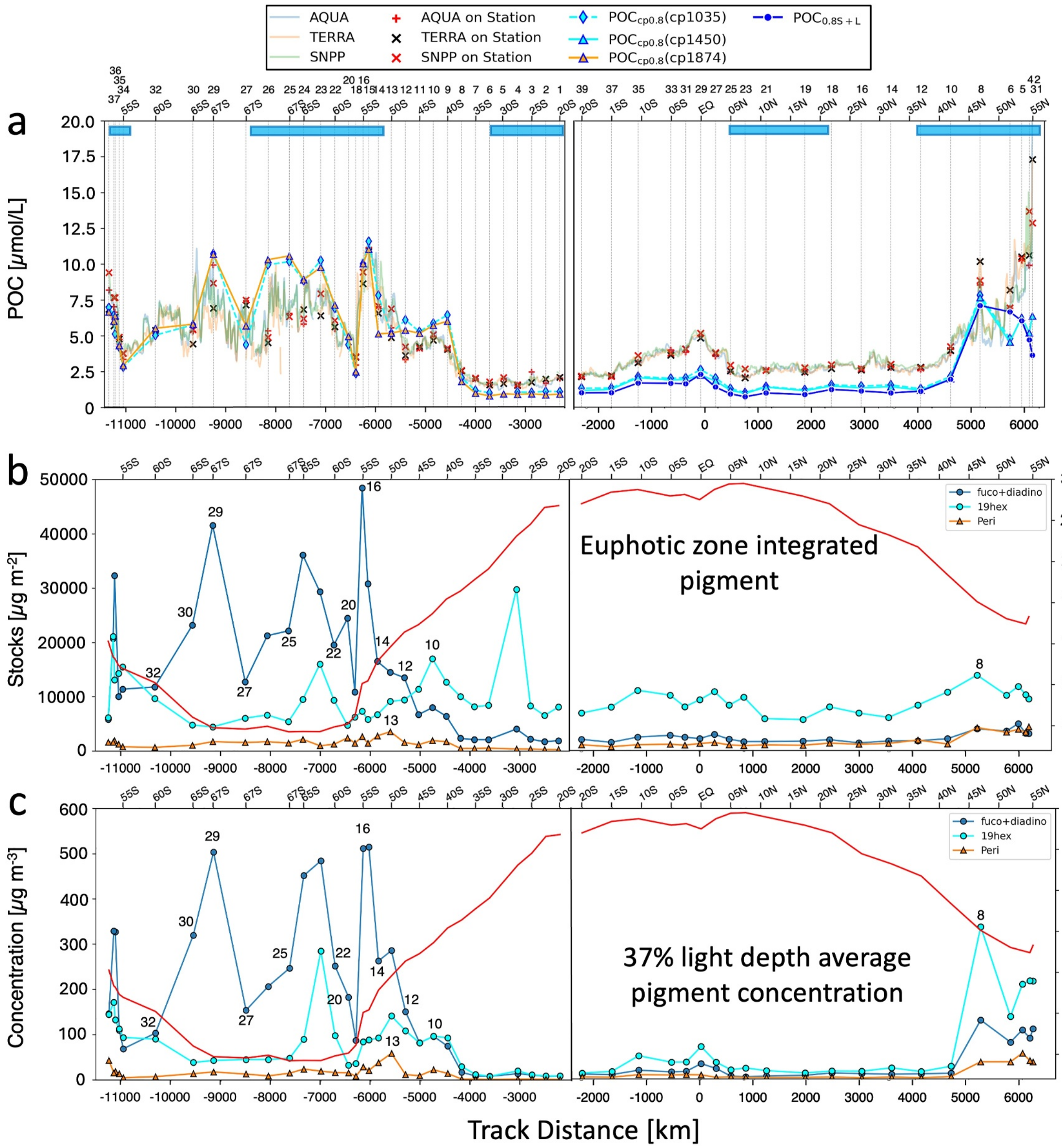


**Figure 10.** (a) Comparison of AQUA, TERRA, and SNPP satellite retrievals of surface layer $POC_{SAT}$, $POC_{0.8S+L}$ (GP15 only), and $POC_{cp0.8}$. $POC_{0.8S+L}$ and $POC_{cp0.8}$ are averaged over one light attenuation depth. The blue bars denote areas of low satellite retrievals, (b) euphotic zone integrated pigment biomarker stocks for fucoxanthin+diadinoxanthin (diatoms), for 19'-hexanoyloxyfucoxanthin (coccolithophores) and peridinin (dinoflagellates), and (c) average pigment concentrations over the first light attenuation depth. 19'-hex signals south of the APF are from the haptophyte *Phaeocystis*.

The two-band color index algorithm ($PIC_{CI2}$, Mitchell et al., 2017) estimates PIC concentrations using the reflectance difference between 547 and 667 nm. This algorithm is improved over the 2B/3B algorithm as it is more resistant to both atmospheric correction errors and residual errors in sun glint corrections. Mitchell et al. (2017) also compared the $PIC_{CI2}$ to the $PIC_{2B/3B}$ and in situ PIC along a meridional transect (from ~50°N to ~50°S) in the Atlantic Ocean. They found that $PIC_{CI2}$ is consistently higher than $PIC_{2B/3B}$, but in better agreement with the in situ observations except in the vicinity of dust impacted areas near the equator.

In our study, $PIC_{CI2}$ has slightly better coverage than the $PIC_{2B/3B}$ (Figure S6 in Supporting Information S1). For example, at GP17 S20, the $PIC_{2B/3B}$ algorithm failed to retrieve any data from three satellites, but the $PIC_{CI2}$ algorithm was completely successful. Similar to Mitchell et al. (2017), $PIC_{CI2}$ is consistently higher than $PIC_{2B/3B}$ (Figure S1 in Supporting Information S1). For GP15 observations in the subarctic north Pacific, $PIC_{CI2}$ is better aligned with in situ data (Figure 8) while $PIC_{2B/3B}$ underestimates; however, from the North Pacific Gyre to the

APF, $PIC_{2B/3B}$ is in close agreement with both McLane sample $PIC_{S+L}$ and $PIC_{\beta}$ whereas $PIC_{CI2}$ is 100–200 nM higher than $PIC_{S+L}$. We hypothesize that overestimation of $PIC_{CI2}$ arises because it was calibrated using a dataset predominantly from the Atlantic without representation of waters from the oligotrophic Pacific Ocean.

### 4.3. Particle Birefringence in Waters Near the Antarctic Polar Front

The source of particle birefringence in waters north and south of the Antarctic Polar Front may be different. South of the APF, stations S20 through S29 clearly show a strong non-carbonate source of particle birefringence.

North of the APF, at GP17 S14 (52.3°S), polarized microscope analysis of the material on the prefilter of the 25 m sample did confirm the dominance of coccolithophores and foraminifera carbonate particles as the source of measured birefringence (Figure 5); Although there was no "QMA" holder sample from 25 m, analysis of material from the McLane "SUPOR" holder yielded a $PIC_{S+L}$ concentration of 83 nM at 25 m. This value is 100 nM lower than the upcast $PIC_{\beta}$ value of 195 nM and we cannot completely rule out the possibility that there was some additive non-carbonate signal at S14; Satellite $PIC_{2B/3B}$ and $PIC_{CI2}$ were 350 and 520 nM higher than $PIC_{S+L}$, respectively at the same location. Below 70 m, $PIC_{\beta}$ and $PIC_{S+L}$ concentrations were elevated throughout the water column compared to other stations and both $PIC_{\beta}$ and $PIC_{S+L}$ rose to 150 nM in the near bottom nepheloid layer near 3,800 m. This deep value was the highest recorded at any station in the combined GP15 (see, e.g. Bishop et al., 2022) and GP17 transects.

Transmitted and cross-polarized light microscopy of 1–51 μm samples from S25 (67°S) and >51 μm material from S25 and S29 (Figures 5 and 6) confirmed the dominance of diatoms and a complete absence of coccolithophores and coccoliths. Interestingly, our microscopy found that calcareous foraminifera and pteropods were present in samples from S25 and S29: few at S25 and relatively high numbers at S29, consistent with trends of sample $PIC_{S+L}$ values. It is unreasonable to assume that the PIC sensor is 4–5 times more sensitive to foraminifera and pteropod PIC. For this reason, there must an additive interference from another source. Phytoplankton pigment data from GP15 and GP17 show that coccolithophores are a major species compared to diatoms everywhere north of 45°S (Figure 10c). Diatom markers peaked at stations S16 and S29.

### 4.4. Interference of OBCP Optical Proxies in the Southern Ocean

In the coldest waters of the Southern Ocean, the low PIC measured in size-fractionated pump samples is consistent with previous observations in the Subpolar Region, including both size-fractionated large volume particle samples ($PIC_{S+L} < 20$ nM, Lam & Bishop, 2007) and PIC measured using the acid-labile backscattering method (Balch et al., 2016). However, both satellite $PIC_{2B/3B}$ and sensor $PIC_{\beta}$ are far higher than sample $PIC_{S+L}$ (Figure 8) with sensor $PIC_{\beta}$ overestimating $PIC_{S+L}$ by up to 350 nM and $PIC_{2B/3B}$ and $PIC_{CI}$ overestimating in the same waters by up to 500 nM and >700 nM, respectively. Are there unidentified or under-appreciated birefringence sources in Southern Ocean surface waters? Is there overlap between these birefringent effects and uncorrected sources of error in the satellite algorithms for this critical region?

#### 4.4.1. Anomalous $PIC_{\beta}$ Data

Clay minerals are birefringent particles but are only abundant in the surface ocean near continental margins and thus are ruled out. $SrSO_4$ (celestite, *Acantharia*), another birefringent biomineral, was observed at concentrations higher than 1 nM in the upper 100 m at 66°S during the Southern Ocean Iron Experiment (SOFeX) (Lam & Bishop, 2007) but its birefringence is 10 times lower than both calcite or aragonite (Guay & Bishop, 2002) and concentrations are nearly 2 orders of magnitude lower than our birefringence PIC signal. Birefringent fragments of fish scales ($CaPO_4$) are large and would be rejected as spikes in our profiles. It has been also suggested that there are birefringent chromosomes in some dinoflagellate taxa (Cachon et al., 1989). Our microscopic analysis confirmed that dinoflagellates were present in surface waters at S14 but also that calcareous organisms were far more abundant.

Biogenic silica occurs in high concentrations in the >51 μm size fraction at 66°S in SOFeX samples, consistent with abundant chain forming diatoms (Lam & Bishop, 2007), however, biogenic silica has no birefringence (Guay & Bishop, 2002). During the GP17 cruise, the continuous in-line flow cyto-bot (IFCB) imagery of surface water indicated that lightly silicified diatoms become present in the Subantarctic Zone, and heavily silicified diatom

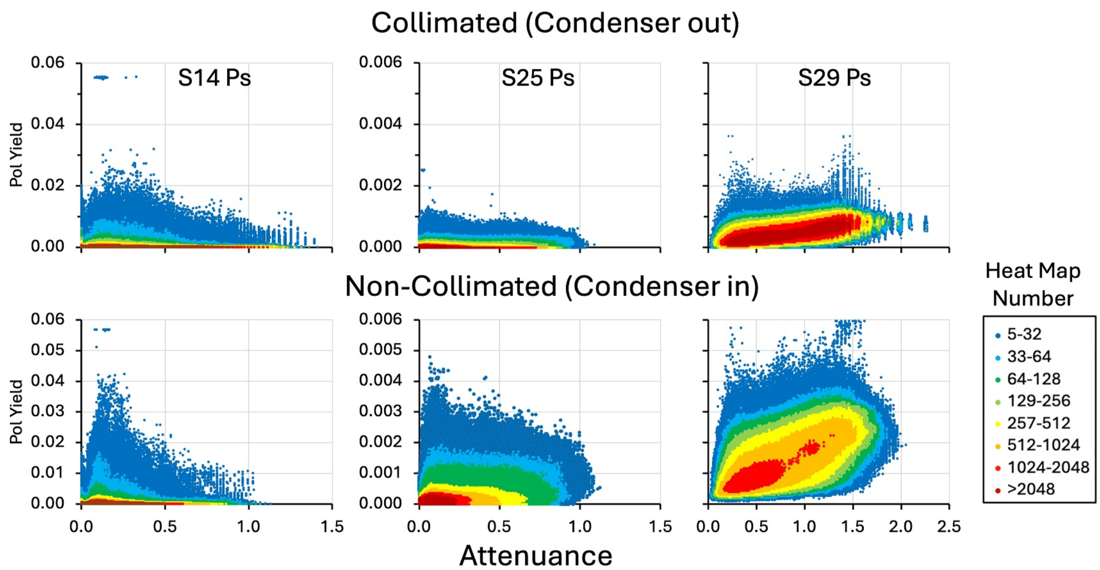


**Figure 11.** Analysis of the relationship between Polarization Yield and Attenuance in images of prefilter material taken from Stations 14, 25, and 29. Two illumination conditions were used, condenser out (collimated illumination) of the sample and condenser in (non-collimated, a cone shaped illumination of the sample, ~30° angle). Aperture setting was 0.5. Results show that polarization yield and attenuance were not correleated in either sample from S14 and S25. These properties were correlated in the sample from S29, dominated with heavily silicified colony-forming diatoms. The Polarization Yield scale is magnified 10*X* for samples from S25, and S29.

taxa such as *Fragilariopsis* (a chain-forming diatom) and *Coscinodiscus* were observed in the Polar Frontal Zone (Twining et al., 2023).

All light reflecting from particle surfaces takes on polarization, but in the case of the PIC sensor most of reflected light should be scattered away from its collimated beam and thus not detected. The only way for a signal to arise is through multiple scattering which would direct the reflected light in the forward direction. We argue that forward internal reflections of light by voids or cellular structures within frustules of some members of heavily silicified colony-forming diatoms are the source of the anomalous $PIC_\beta$ signal (Figures 5 and 6). Indeed, at GP17 S29 (67°S) we found very high abundances of *Fragilariopsis* and *Pseudo-nitzschia* diatom colonies (Figures S12 and S13 in Supporting Information S1) exactly where the highest anomalous euphotic zone $PIC_\beta$ concentrations were found; S29 was also the station which had the deepest mixed layer (sigma-theta difference of 0.05 at 65 m, Figure 8d). All stations with surface waters colder than 1°C were anomalous.

Figure 11 shows heat maps of polarization yield against attenuance derived from calibrated transmitted and cross-polarized transmitted light images of McLane Prefilter samples at 0.5 μm resolution. Waters for all three samples had nearly identical measures of beam attenuation coefficient, and fluorescence.

Given the above findings, we hypothesize that heavily silicified colony-forming diatoms form micro-bubbles within some colony members to achieve positive buoyancy in the weakly stratified environment in which they live. Alternatively, the packing arrangement of some diatom species may enable bubble entrapment and thus a buoyancy gain.

### 4.4.2. Anomalous Satellite Data

Can the anomalously high satellite $PIC_{2B/3B}$ and $PIC_{CI2}$ concentrations retrieved south of the polar front also be explained? This interference arises from non-carbonate backscattering sources. In the Antarctic waters, PIC was only 1% of bSi on a molar basis (Lam & Bishop, 2007; Trull et al., 2018). Although having a lower refractive index than calcium carbonate, literature suggests biogenic silica can produce abnormally high backscattering when diatoms are present in high abundance (Broerse et al., 2003). We hypothesize that direct bubble formation/entrapment by colonial diatoms to enhance buoyancy would further enhance backscattering. Bubble injection from breaking waves could be another scattering source. Wind speed data during the GP17 expedition indicated relatively high wind speeds (>10 m/s) from 56 to 65°S, which would lead to a surface water air bubble void fraction ranging from $2 \times 10^{-6}$ to $4 \times 10^{-5}$. In the Southern Ocean where chlorophyll-a concentration is around 0.5 mg $m^{-3}$, such bubble void fractions can produce 50%–100% of optical scatter compared to that from chlorophyll (Terrill et al., 2001).

### 4.5. Southern Boundary of Coccolithophores as the Key to Improve Satellite Estimated PIC

A frequently used rule of thumb is that coccolithophores with calcium carbonate architecture, that is, high PIC, are rarely found in waters colder than 5°C. Most studies of plankton assemblages in different sectors of the southern hemisphere have proved the southern boundary of coccolithophores is usually between the Antarctic Polar Front and Southern ACC Front (Beaufort et al., 2011; Eynaud et al., 1999; Mohan et al., 2008; Nishida, 1986). Furthermore, the decline of coccolithophores leads to a sharp transition of biominerals from PIC to biogenic silica (bSi), that is, low PIC, south of the polar frontal zone (Balch et al., 2011, 2016; Lam & Bishop, 2007); The increasing abundance of diatoms is suggested to be associated with the poleward rise in iron availability and nutrient supply (Balch et al., 2016), as well as the decrease in SST, which is unfavorable for *E. huxleyi*, the most common species of coccolithophores in high latitude seas. In our data, we found little or no coccolithophore PIC present south of the APF, consistent with other studies above.

A recent study (Winter et al., 2014) suggested *E. huxleyi* is more sensitive to SST and salinity than to ocean carbon chemistry, because it is less competitive acquiring CO2(aq) due to less efficient Rubisco enzyme compared to other algae (e.g., diatoms). Given that coccolithophores are rarely found south of the sACCF, we propose that SST can serve as an indicator of non-PIC scattering in the Southern Ocean. In our case, 5°C remains a reasonable threshold below which satellite PIC should be ignored. Further research and synthesis on the southern boundary of coccolithophores in the Southern Ocean is necessary to refine the threshold of filtering algorithm for satellite derived PIC product.

## 5. Conclusions

In this study, we have focused on the quantification of the biological carbon pump by synthesizing satellite and in situ optical proxies for PIC and POC and analytical measurements in large-volume particulate samples collected from GEOTRACES transects in the Pacific Ocean from Alaska to the Southern Ocean. To facilitate the analysis, we have developed an improved scheme that significantly improves the temporal and spatial matchup of satellite and shipboard data. We presented the first transect for PIC spanning latitudes from 56°N to 67°S in the Pacific Ocean and the Pacific sector of the Southern Ocean, that is derived from in situ measurements of birefringence photon yield.

Our findings reveal distinct patterns of PIC distribution correlating with oceanographic fronts and nutrient availability. In the "Great Calcite Belt", high abundance of PIC was found in the Subantarctic Zone and Polar Frontal Zone where nitrate concentrations are elevated and where sea surface temperatures are above 5°C (Figures 7a and 7b). Elevated concentrations of PIC well below the euphotic zone indicated enhanced export in the region of GP17 stations 12–16 from 45°S to 55°S. Similar indications of enhanced export were seen south of the subarctic front between 45°N and 35°N and at the equatorial divergence zone. The elevated PIC in sub-euphotic zone waters in these regions is the result of the breakup of sinking aggregates exported from regions of high photosynthetic calcification. In the coldest surface waters of the Southern Ocean south of the polar front, large-volume particulate samples indicate that PIC is absent or at low levels (highest: 60 nM at S29) but that these concentrations arise from calcified foraminifera and pteropods.

Comparison between satellite PIC and McLane samples reveals that strong biases exist in the satellite data for the Southern Ocean. Satellite PIC algorithms appear to include interference from other scattering sources such as highly abundant biogenic silica, diatom-entrapped air bubbles, and/or micro-bubbles caused by high wind speeds. Particulate samples from the subtropical Pacific and the Pacific sector of the Southern Ocean are needed to account for known factors—such as coccolith morphology and the partitioning of PIC between living coccolithophores and coccoliths—and to isolate suspected non-PIC scattering sources that appear to contribute to satellite-detected radiances.

Two prototype PIC sensors demonstrated reliable and consistent operation in profiles extending to depths as great as 6,000 m and temperatures ranging from −1.5°C to 29°C. They exhibited strong agreement with McLane sample measurements, particularly in oligotrophic waters where PIC concentrations were low. However, the sensor's accuracy in surface waters varied with latitude and PIC concentration. The birefringence sensor may underestimate PIC in subarctic and subantarctic surface waters where a high fraction of carbonate may be in living coccolithophores such that cellular material would block a fraction of the signal. GP17 stations 10 and 35 fell into this category, but also lacked in contemporaneous profile and sample observations. In deeper waters sample and sesnor PIC were aligned. Further microscopic analysis of the complete suite of near surface McLane samples from GP15 and GP17-OCE would further illuminate these issues.

There is no doubt that the PIC sensor detected high birefringence signals in the Southern Ocean's shallow euphotic zone, where samples suggest little PIC is present; however, the sensor matched sample data below the euphotic zone. We have ruled out birefringent clay minerals and $SrSO_4$ phases as causes of this interference. Microscopy has ruled out a significant birefringence from dinoflagellates whose pigment systematics were furthermore a poor match to our anomalous trends. Multiple lines of evidence point to a false birefringence signal arising from additive stray polarized light by colony/chain-forming diatoms when they dominate in surface waters. This birefringence is hypothesized to result from buoyancy enhancing voids or other birefringent cellular elements within some members of such colonies as an ecological adaption to the poorly stratified near freezing environment (e.g., low light and a 65 m deep mixed layer at GP17-S29) in which they live. Culture studies of Antarctic colony-forming diatoms at −1 to 1°C temperatures would answer the question of buoyancy and birefringence.

Our transmissometer-derived POC proxy ($POC_{cp0.8}$) showed good agreement with large volume particle POC samples from GP15. However, satellite-derived $POC_{SAT}$ estimates exhibited systematic positive offsets in the oligotrophic gyres (compared to both sample POC and sensor $POC_{0.8}$) due to a known elevated contribution to POC by picoplankton smaller than 0.8 μm. McLane pump sample analyses for major particle phases, including POC, is in progress for GP17 and will further inform the understanding of these optical proxies.

Evidence presented above suggests that optical transmission and cross-polarized light proxies for POC and PIC concentrations, respectively, are understood well enough to merit long-term deployment on autonomous platforms. Given the numerous insights our prototype sensors for PIC have yielded, these results provide strong justification for further engineering work and commercialization of the sensor. Transmissometer sensors have indeed been deployed on Carbon Explorer floats (e.g., Bishop & Wood, 2009) in the extreme southern ocean. Both transmissometer and birefringence sensors will be deployed on the OCOs and will enable simultaneous real time measurement of POC and PIC concentrations and flux (including particle size-distributions and classes) to kilometer depths on a daily basis for seasons to years. Autonomous sensor systems, such as the OCO, are ideally suited for deployment in the dangerous regimes such as subarctic and subantarctic regions where PIC and POC export are both strong and dynamic and time series is needed. Paired with ongoing improvements in satellite-derived algorithms, these efforts promise continued large increases in our understanding of ocean ecology and carbon dynamics.

Finally, there is a large community of scientists using global satellite data sets to infer ocean biological processes and our analysis provides a unique insight to the use of such data. For example, Lacour et al. (2023) analyzed BioARGO float data and found indications of high carbon export in the Southern Ocean which were linked to satellite observations of a coccolithophore bloom. Our assessment of the context of the imagery is that the anomalous coccolithophore bloom appears to be due to diatoms and not coccolithophores.

An improved estimate of global PIC stocks can be achieved through a quality controlled satellite PIC product, synthesized from multiple satellites. Our study shows that PIC retrieved from 4 km 8 day satellite composites are prone to subpixel-scale contamination (Figure 7a), such as from sub-pixel scale clouds; and that this can occur at all latitudes. These contaminated data are currently composited into monthly and annual fields. We recommend that such PIC stock estimates utilize 8 day imagery from multiple satellites, whereby inconsistent retrievals are excluded. Furthermore we note that cloud contamination presents a major challenge in estimating global PIC stocks, particularly in regions like the Great Calcite Belt, which accounts for 26% of global suspended PIC (Balch et al., 2005). In our study, a simple 2D temporal/spatial interpolation method has doubled retrievals in these regions. We further recommend using SST warmer than 5°C as a threshold for future retrieval algorithms.

## Data Availability Statement

All datasets from this study will be available through the international GEOTRACES program and will be archived at the relevant NSF data repositories including the Biological and Chemical Oceanography Data Management Office (BCO-DMO).

GEOTRACES GP 15 CTD optics data sets are Bishop and Lam (2024) and Bishop, Lam, and Cutter (2025); McLane pump sample data are Lam et al. (2024a, 2024b). GEOTEACES GP17-OCE CTD optics data sets are Bishop, Ohnemus, and Lam (2025), Bishop, Cutter, and Ohnemus (2025), and Bishop and Twining (2025); McLane pump sample data are Lam (2024).

**Acknowledgments**

This study was supported by NSF-OCE 2123942 to JKB, NSF-OCE 2049297 to PJL, and NSF-OCE 2049341 to DCO. NSF OCE-2023315 (Greg Cutter, ODU) supported GTC_CTD deployments during GP17-OCE. We would like to thank the officers, crew and scientific party members aboard *R.V. Revelle* during the 2018 GEOTRACES GP15 and 2022 GEOTRACES GP17-OCE cruises for help during all aspects of our operations. The International GEOTRACES Program is possible in part thanks to the support from the U.S. National Science Foundation (OCE-2140395) to the Scientific Committee on Oceanic Research (SCOR). At UCSC, Isabelle Maru Shapiro performed analysis of McLane Samples for PIC with help from Thao Vy Le. At UC Berkeley, Drs. Rudy Wenk and Matthew Gleason enabled our light microscopic and SEM analysis. Seabird Scientific contributed probono service support for our PIC sensors. We also acknowledge the NASA Ocean Color group for the satellite data used in this work.

## References

Armstrong, R. A., Lee, C., Hedges, J. I., Honjo, S., & Wakeham, S. G. (2001). A new, mechanistic model for organic carbon fluxes in the ocean based on the quantitative association of POC with ballast minerals. *Deep Sea Research Part II: Topical Studies in Oceanography*, *49*(1–3), 219–236. https://doi.org/10.1016/S0967-0645(01)00101-1

Balch, W. M., Bates, N. R., Lam, P. J., Twining, B. S., Rosengard, S. Z., Bowler, B. C., et al. (2016). Factors regulating the great calcite Belt in the Southern Ocean and its biogeochemical significance. *Global Biogeochemical Cycles*, *30*(8), 1124–1144. https://doi.org/10.1002/2016GB005414

Balch, W. M., Bowler, B. C., Drapeau, D. T., Lubelczyk, L. C., & Lyczkowski, E. (2018). Vertical distributions of coccolithophores, PIC, POC, biogenic silica, and chlorophyll a throughout the global ocean. *Global Biogeochemical Cycles*, *32*, 2–17. https://doi.org/10.1002/2016GB005614

Balch, W. M., Drapeau, D. T., Bowler, B. C., Lyczskowski, E., Booth, E. S., & Alley, D. (2011). The contribution of coccolithophores to the optical and inorganic carbon budgets during the Southern Ocean Gas Exchange Experiment: New evidence in support of the "Great Calcite Belt" hypothesis. *Journal of Geophysical Research*, *116*, C00F06. https://doi.org/10.1029/2011JC006941

Balch, W. M., Gordon, H. R., Bowler, B. C., Drapeau, D. T., & Booth, E. S. (2005). Calcium carbonate measurements in the surface global ocean based on Moderate-Resolution Imaging Spectroradiometer data. *Journal of Geophysical Research*, *110*(C7), 2004JC002560. https://doi.org/10.1029/2004JC002560

Beaufort, L., Probert, I., De Garidel-Thoron, T., Bendif, E. M., Ruiz-Pino, D., Metzl, N., et al. (2011). Sensitivity of coccolithophores to carbonate chemistry and ocean acidification. *Nature*, *476*(7358), 80–83. https://doi.org/10.1038/nature10295

Berelson, W. M., Balch, W. M., Najjar, R., Feely, R. A., Sabine, C., & Lee, K. (2007). Relating estimates of $CaCO_3$ production, export, and dissolution in the water column to measurements of $CaCO_3$ rain into sediment traps and dissolution on the sea floor: A revised global carbonate budget. *Global Biogeochemical Cycles*, *21*(1), 2006GB002803. https://doi.org/10.1029/2006GB002803

Bishop, J. K. B. (2009). Autonomous observations of the Ocean biological carbon pump. *Oceanography*, *22*(2), 182–193. https://doi.org/10.5670/oceanog.2009.48

Bishop, J. K. B., Amaral, V. J., Lam, P. J., Wood, T. J., Lee, J.-M., Laubach, A., et al. (2022). Transmitted cross-polarized light detection of particulate inorganic carbon concentrations and fluxes in the Ocean water column: Ships to ARGO floats. *Frontiers in Remote Sensing*, *3*, 837938. https://doi.org/10.3389/frsen.2022.837938

Bishop, J. K. B., Calvert, S. E., & Soon, M. Y. S. (1998). Spatial and temporal variability of POC in the northeast Subarctic Pacifc.

Bishop, J. K. B., Cutter, G. A., & Ohnemus, D. C. (2025). Cross-polarized photon yield, beam attenuation coefficient, and fluorescence data derived from optical particle sensors deployed during casts of the GTC rosette on the GP17-OCE R/V Roger Revelle (RR2214) cruise Dec 2022 - Jan 2023. Biological and Chemical Oceanography Data Management Office (BCO-DMO). (Version 1) Version Date 2025-03-17. https://doi.org/10.26008/1912/bco-dmo.956233.1

Bishop, J. K. B., & Lam, P. J. (2024). Particle birefringence photon yield and particle beam attenuation coefficient derived from a logging CTD deployed during McLane Pump casts on the US GEOTRACES Pacific Meridional Transect (PMT) cruise (GP15) on R/V Roger Revelle from Sept-Nov 2018. Biological and Chemical Oceanography Data Management Office (BCO-DMO). (Version 1) Version Date 2024-12-01. https://doi.org/10.26008/1912/bco-dmo.941463.1

Bishop, J. K. B., Lam, P. J., & Cutter, G. A. (2025). Particle birefringence photon yield and particle beam attenuation coefficient derived from optical particle sensors deployed on GTC CTD casts on the U.S. GEOTRACES Pacific Meridional Transect (PMT) cruise (GP15) on R/V Roger Revelle from Sept-Nov 2018. Biological and Chemical Oceanography Data Management Office (BCO-DMO). (Version 1) Version Date 2025-02-04. https://doi.org/10.26008/1912/bco-dmo.941657.1

Bishop, J. K. B., Lam, P. J., & Wood, T. J. (2012). Getting good particles: Accurate sampling of particles by large volume in-situ filtration. *Limnology and Oceanography: Methods*, *10*(9), 681–710. https://doi.org/10.4319/lom.2012.10.681

Bishop, J. K. B., Ohnemus, D. C., & Lam, P. J. (2025). Cross-polarized photon yield, beam attenuation coefficient, scattering, and fluorescence data derived from optical particle sensors interfaced to a CTD deployed during McLane pump casts on the GP17-OCE R/V Roger Revelle (RR2214) cruise Dec 2022 - Jan 2023. Biological and Chemical Oceanography Data Management Office (BCO-DMO). (Version 1) Version Date 2025-03-13. https://doi.org/10.26008/1912/bco-dmo.956099.1

Bishop, J. K. B., & Twining, B. (2025). Beam attenuation coefficient, scattering, and fluorescence data derived from optical particle sensors deployed during casts of the ODF rosette on the GEOTRACES GP17-OCE cruise aboard R/V Roger Revelle (RR2214) from December 2022 to January 2023. Biological and Chemical Oceanography Data Management Office (BCO-DMO). (Version 1) Version Date 2025-03-13. https://doi.org/10.26008/1912/bco-dmo.949808.1

Bishop, J. K. B., & Wood, T. J. (2008). Particulate matter chemistry and dynamics in the twilight zone at VERTIGO ALOHA and K2 sites. *Deep Sea Research Part I: Oceanographic Research Papers*, *55*(12), 1684–1706. https://doi.org/10.1016/j.dsr.2008.07.012

Bishop, J. K. B., & Wood, T. J. (2009). Year round observations of carbon biomass and flux variability in the Southern Ocean. *Global Biogeochemical Cycles*, *23*(2), GB2019. https://doi.org/10.1029/2008GB003206

Bishop, J. K. B., & Wood, T. J. (2024). *The Ocean carbon observer: A fully autonomous ARGO-style float for year round observations of particulate organic and inorganic concentrations and fluxes in remote and stormy seas*. Presented at the 2024 Ocean Sciences Meeting, American Geophysical Union.

Bourne, H. L., Bishop, J. K. B., Connors, E. J., & Wood, T. J. (2021). Carbon export and fate beneath a dynamic upwelled filament off the California coast. *Biogeosciences*, *18*(10), 3053–3086. https://doi.org/10.5194/bg-18-3053-2021

Boyd, P. W., Claustre, H., Levy, M., Siegel, D. A., & Weber, T. (2019). Multi-faceted particle pumps drive carbon sequestration in the ocean. *Nature*, *568*(7752), 327–335. https://doi.org/10.1038/s41586-019-1098-2

Boyd, P. W., & Trull, T. W. (2007). Understanding the export of biogenic particles in oceanic waters: Is there consensus? *Progress in Oceanography*, *72*(4), 276–312. https://doi.org/10.1016/j.pocean.2006.10.007

Broerse, A. T. C., Tyrrell, T., Young, J. R., Poulton, A. J., Merico, A., Balch, W. M., & Miller, P. I. (2003). The cause of bright waters in the Bering Sea in winter. *Continental Shelf Research*, *23*(16), 1579–1596. https://doi.org/10.1016/j.csr.2003.07.001

Cachon, J., Sato, H., Cachon, M., & Sato, Y. (1989). Analysis by polarizing microscopy of chromosomal structure among dinoflagellates and its phyiogenetic involvement. *Biology of the Cell*, *65*(1), 51–60. https://doi.org/10.1111/j.1768-322X.1989.tb00770.x

Clements, D. J., Yang, S., Weber, T., McDonnell, A. M. P., Kiko, R., Stemmann, L., & Bianchi, D. (2023). New estimate of organic carbon export from optical measurements reveals the role of particle size distribution and export horizon. *Global Biogeochemical Cycles*, *37*(3), e2022GB007633. https://doi.org/10.1029/2022GB007633

Eynaud, F., Giraudeau, J., Pichon, J.-J., & Pudsey, C. J. (1999). Sea-surface distribution of coccolithophores, diatoms, silicoflagellates and dinoflagellates in the South Atlantic Ocean during the late austral summer 1995. *Deep Sea Research Part I: Oceanographic Research Papers*, *46*(3), 451–482. https://doi.org/10.1016/S0967-0637(98)00079-X

Falkowski, P. G., & Raven, J. A. (2007). *Aquatic photosynthesis* (2.). Princeton University Press.

Feely, R. A., Doney, S. T. C., & Cooley, S. A. R. (2009). Ocean acidification: Present conditions and future changes in a high CO2 world. *Oceanography*, *22*(4), 36–47. https://doi.org/10.5670/oceanog.2009.95

Feely, R. A., Sabine, C. L., Lee, K., Berelson, W., Kleypas, J., Fabry, V. J., & Millero, F. J. (2004). Impact of anthropogenic $CO_2$ on the $CaCO_3$ system in the oceans. *Science*, *305*(5682), 362–366. https://doi.org/10.1126/science.1097329

Field, C. B., Behrenfeld, M. J., Randerson, J. T., & Falkowski, P. (1998). Primary production of the biosphere: Integrating terrestrial and oceanic components. *Science*, *281*(5374), 237–240. https://doi.org/10.1126/science.281.5374.237

Gordon, H. R., Boynton, G. C., Balch, W. M., Groom, S. B., Harbour, D. S., & Smyth, T. J. (2001). Retrieval of coccolithophore calcite concentration from SeaWiFS Imagery. *Geophysical Research Letters*, *28*(8), 1587–1590. https://doi.org/10.1029/2000GL012025

Gordon, H. R., & McCluney, W. R. (1975). Estimation of the depth of sunlight penetration in the sea for remote sensing. *Applied Optics*, *14*(2), 413. https://doi.org/10.1364/AO.14.000413

Guay, C. K. H., & Bishop, J. K. B. (2002). A rapid birefringence method for measuring suspended CaCO3 concentrations in seawater. *Deep Sea Research Part I: Oceanographic Research Papers*, *49*(1), 197–210. https://doi.org/10.1016/S0967-0637(01)00049-8

Henson, S. A., Sanders, R., Madsen, E., Morris, P. J., Le Moigne, F., & Quartly, G. D. (2011). A reduced estimate of the strength of the ocean's biological carbon pump: Biological carbon pump strength. *Geophysical Research Letters*, *38*(4). n/a-n/a. https://doi.org/10.1029/2011GL046735

Hu, C., Lee, Z., & Franz, B. (2012). Chlorophyll *a* algorithms for oligotrophic oceans: A novel approach based on three-band reflectance difference. *Journal of Geophysical Research*, *117*(C1), 2011JC007395. https://doi.org/10.1029/2011JC007395

Lacour, L., Llort, J., Briggs, N., Strutton, P. G., & Boyd, P. W. (2023). Seasonality of downward carbon export in the Pacific Southern Ocean revealed by multi-year robotic observations. *Nature Communications*, *14*(1), 1278. https://doi.org/10.1038/s41467-023-36954-7

Lam, P. J. (2024). Size-fractionated particulate inorganic carbon (PIC) in particles collected by in-situ filtration on the US GEOTRACES GP17-OCE cruise on R/V Roger Revelle (RR2214) in the South Pacific and Southern Oceans from December 2022 to January 2023. Biological and Chemical Oceanography Data Management Office (BCO-DMO). (Version 1) Version Date 2024-12-10. http://lod.bco-dmo.org/id/dataset/945724

Lam, P. J., & Bishop, J. K. B. (2007). High biomass, low export regimes in the Southern Ocean. *Deep Sea Research Part II: Topical Studies in Oceanography*, *54*(5–7), 601–638. https://doi.org/10.1016/j.dsr2.2007.01.013

Lam, P. J., Doney, S. C., & Bishop, J. K. B. (2011). The dynamic ocean biological pump: Insights from a global compilation of particulate organic carbon, CaCO $_3$, and opal concentration profiles from the mesopelagic: The dynamic ocean biological pump. *Global Biogeochemical Cycles*, *25*(3). n/a-n/a. https://doi.org/10.1029/2010GB003868

Lam, P. J., Lee, J., Amaral, V. J., Laubach, A., Carracino, N., Rojas, S., & Mateos, K. (2024a). Size-fractionated major, minor, and trace particle composition and concentration from Leg 1 (Seattle, WA to Hilo, HI) of the US GEOTRACES Pacific Meridional Transect (PMT) cruise (GP15, RR1814) on R/V Roger Revelle from Sept to Oct 2018. Biological and Chemical Oceanography Data Management Office (BCO-DMO). (Version 1) Version Date 2024-01-30. https://doi.org/10.26008/1912/bco-dmo.918811.1

Lam, P. J., Lee, J., Amaral, V. J., Laubach, A., Carracino, N., Rojas, S., & Mateos, K. (2024b). Size-fractionated major, minor, and trace particle composition and concentration from Leg 2 (Hilo, HI to Papeete, French Polynesia) of the US GEOTRACES Pacific Meridional Transect (PMT) cruise (GP15, RR1815) on R/V Roger Revelle from Oct to Nov 2018. Biological and Chemical Oceanography Data Management Office (BCO-DMO). (Version 1) Version Date 2024-01-30. https://doi.org/10.26008/1912/bco-dmo.919139.1

Lam, P. J., Lee, J.-M., Heller, M. I., Mehic, S., Xiang, Y., & Bates, N. R. (2018). Size-fractionated distributions of suspended particle concentration and major phase composition from the U.S. GEOTRACES Eastern Pacific Zonal Transect (GP16). *Marine Chemistry*, *201*, 90–107. https://doi.org/10.1016/j.marchem.2017.08.013

Lam, P. J., & Xiang, Y. (2025). The geochemistry of marine particles. In *Treatise on geochemistry* (pp. 459–477). Elsevier. https://doi.org/10.1016/B978-0-323-99762-1.00053-X

Mitchell, C., Hu, C., Bowler, B., Drapeau, D., & Balch, W. M. (2017). Estimating particulate inorganic carbon concentrations of the global Ocean from Ocean Color measurements using a reflectance difference approach. *Journal of Geophysical Research: Oceans*, *122*(11), 8707–8720. https://doi.org/10.1002/2017JC013146

Mohan, R., Mergulhao, L. P., Guptha, M. V. S., Rajakumar, A., Thamban, M., AnilKumar, N., et al. (2008). Ecology of coccolithophores in the Indian sector of the Southern Ocean. *Marine Micropaleontology*, *67*(1–2), 30–45. https://doi.org/10.1016/j.marmicro.2007.08.005

Nishida, S. (1986). Nannoplankton flora in the Southern Ocean, with special reference to siliceous varieties. *Memoirs of National Institute of Polar Research - Special Issue*(40), 56–68.

Okada, H., & Honjo, S. (1973). The distribution of oceanic coccolithophorids in the Pacific. *Deep-Sea Research and Oceanographic Abstracts*, *20*(4), 355–374. https://doi.org/10.1016/0011-7471(73)90059-4

Orsi, A. H., Whitworth, T., & Nowlin, W. D. (1995). On the meridional extent and fronts of the Antarctic Circumpolar Current. *Deep Sea Research Part I: Oceanographic Research Papers*, *42*(5), 641–673. https://doi.org/10.1016/0967-0637(95)00021-W

Owens, S. A., Pike, S., & Buesseler, K. O. (2015). Thorium-234 as a tracer of particle dynamics and upper ocean export in the Atlantic Ocean. *Deep Sea Research Part II: Topical Studies in Oceanography*, *116*, 42–59. https://doi.org/10.1016/j.dsr2.2014.11.010

Patil, S. M., Mohan, R., Shetye, S. S., Gazi, S., Baumann, K.-H., & Jafar, S. (2017). Biogeographic distribution of extant coccolithophores in the Indian sector of the Southern Ocean. *Marine Micropaleontology*, *137*, 16–30. https://doi.org/10.1016/j.marmicro.2017.08.002

Poulton, A. J., Holligan, P. M., Charalampopoulou, A., & Adey, T. R. (2017). Coccolithophore ecology in the tropical and subtropical Atlantic Ocean: New perspectives from the Atlantic meridional transect (AMT) programme. *Progress in Oceanography*, *158*, 150–170. https://doi.org/10.1016/j.pocean.2017.01.003

Sabine, C. L., Feely, R. A., Gruber, N., Key, R. M., Lee, K., Bullister, J. L., et al. (2004). The oceanic sink for anthropogenic $CO_2$. *Science*, *305*(5682), 367–371. https://doi.org/10.1126/science.1097403

Siegel, D. A., Buesseler, K. O., Doney, S. C., Sailley, S. F., Behrenfeld, M. J., & Boyd, P. W. (2014). Global assessment of ocean carbon export by combining satellite observations and food-web models. *Global Biogeochemical Cycles*, *28*(3), 181–196. https://doi.org/10.1002/2013GB004743

Stramski, D., Reynolds, R. A., Babin, M., Kaczmarek, S., Lewis, M. R., Rottgers, R., et al. (2008). Relationships between the surface concentration of particulate organic carbon and optical properties in the eastern South Pacific and eastern Atlantic Oceans. *Biogeosciences*, *5*(1), 171–201. https://doi.org/10.5194/bg-5-171-2008

Talley, L. D., Pickard, G. L., Emery, W. J., & Swift, J. H. (2011). Southern Ocean. In *Descriptive physical Oceanography* (pp. 437–471). Elsevier. https://doi.org/10.1016/B978-0-7506-4552-2.10013-7

Terrill, E. J., Melville, W. K., & Stramski, D. (2001). Bubble entrainment by breaking waves and their influence on optical scattering in the upper ocean. *Journal of Geophysical Research*, *106*(C8), 16815–16823. https://doi.org/10.1029/2000JC000496

Trull, T. W., Passmore, A., Davies, D. M., Smit, T., Berry, K., & Tilbrook, B. (2018). Distribution of planktonic biogenic carbonate organisms in the Southern Ocean south of Australia: A baseline for ocean acidification impact assessment. *Biogeosciences*, *15*(1), 31–49. https://doi.org/10.5194/bg-15-31-2018

Twining, B. S., Fitzsimmons, J. L., & Cutter, G. A. (2023). U.S. GEOTRACES GP17-OCE cruise report.

Volk, T., & Hoffert, M. I. (1985). Ocean carbon pumps - analysis of relative strengths and efficiencies in ocean-driven atmospheric CO2 changes (pp. 99–110).

Winter, A., Henderiks, J., Beaufort, L., Rickaby, R. E. M., & Brown, C. W. (2014). Poleward expansion of the coccolithophore *Emiliania huxleyi*. *Journal of Plankton Research*, *36*(2), 316–325. https://doi.org/10.1093/plankt/fbt110

Xiang, Y., & Lam, P. J. (2020). Size-fractionated compositions of marine suspended particles in the western Arctic ocean: Lateral and vertical sources. *Journal of Geophysical Research: Oceans*, *125*(8), e2020JC016144. https://doi.org/10.1029/2020JC016144

Yao, X., & Schlitzer, R. (2013). Assimilating water column and satellite data for marine export production estimation. *Geoscientific Model Development*, *6*(5), 1575–1590. https://doi.org/10.5194/gmd-6-1575-2013